

Extraordinary Coulomb correlations and incipient excitonic instability of Weyl fermions

Michihiro Hirata^{1,2}, Kyohei Ishikawa², Genki Matsuno³, Akito Kobayashi³, Kazuya Miyagawa², Masafumi Tamura⁴, Claude Berthier⁵ & Kazushi Kanoda²

¹*Institute for Materials Research, Tohoku University, Aoba-ku, Sendai 980-8577, Japan.*

²*Department of Applied Physics, University of Tokyo, Bunkyo-ku, Tokyo 113-8656, Japan.*

³*Department of Physics, Nagoya University, Chikusa-ku, Nagoya 464-8602, Japan.*

⁴*Department of Physics, Faculty of Science and Technology, Tokyo University of Science, Noda, Chiba 278-8510, Japan.*

⁵*Laboratoire National des Champs Magnétiques Intenses, UPR 3228 CNRS, UJF-UPS-INSA, 38042 Grenoble, France.*

Correspondence and requests for materials should be addressed to M.H. (michihiro_hirata@imr.tohoku.ac.jp) or K.K. (kanoda@ap.t.u-tokyo.ac.jp)

In modern solid-state physics, electron correlations constitute major sources of interests in the exploration of novel electronic properties. For Weyl fermion systems consisted of relativistic massless electrons with nodal dispersion¹, the interparticle Coulomb interaction has a highly unusual characteristic since its long-range component is unscreened at the band-crossing Weyl nodes due to the vanishing density of states², affecting drastically the nature of fermions as established in quantum electrodynamics^{3,4}; indeed, exotic phenomena like excitonic mass generation have been predicted in strong coupling⁵⁻⁷. To characterize how strong the interaction can be and identify what kind of emergent Coulomb-induced phenomena it brings about in real materials is among top priorities over experimental

challenges of addressing “strongly correlated Weyl fermions”². Here, employing nuclear-magnetic-resonance (NMR) spectroscopy, we show that the anisotropic Weyl fermions appearing in a quasi-two-dimensional organic conductor⁸⁻¹⁰ possess an extraordinarily strong Coulomb correlation. We find that this characteristic leads to a tremendous enhancement of the NMR index of spin correlations (the Korringa ratio), given by the ratio of the NMR relaxation rate to the square of the spectral shift, by a factor of $\sim 10^3$ from the values in conventional metals. Our model calculations based on renormalization-group treatment reveal that the observed enormous spin correlation is a general characteristic of Weyl fermion systems, arising from the short-wavelength correlations that persist at low energy despite the drastic suppression of the long-wavelength correlations by the running Coulomb coupling²⁻⁷. On further cooling, the dynamic spin susceptibility (probed by the NMR relaxation rate) shows a sudden increase, which is identified by model calculations within the ladder approximation as indicating spin-triplet excitonic fluctuations – precursors to mass generation associated with chiral symmetry breaking²⁻⁴.

The Weyl fermions (WFs) are novel massless particles in solids exhibiting linear energy-momentum dependence whose low-energy properties can be described by the relativistic Dirac-Weyl theory. They have been discovered in an increasing number of materials in two-dimensional (2D) and three-dimensional (3D) systems¹, where extensive studies focussing mainly upon the relativistic and topological aspects of WFs revealed unconventional charge² and spin⁹⁻¹² responses. However, the detailed mechanisms of Coulomb correlations among interacting WFs have experimentally remained largely elusive. The present work addresses this issue by employing NMR techniques in conjunction with theoretical calculations; the interaction strength

as well as the underlying excitation and correlation mechanisms are directly resolved through investigating the dynamic and static spin susceptibilities.

The system studied here is the organic charge-transfer salt α -(BEDT-TTF)₂I₃ (hereafter abbreviated to α -I₃), which is a novel class of material hosting 2D WFs with two tilted Weyl cones at \mathbf{k}_0 and $-\mathbf{k}_0$ in momentum space^{8,13-15} (Fig. 3c). α -I₃ is a layered material constituted of BEDT-TTF conducting and I₃ insulating layers (Fig. 1a) in which WFs, described by the BEDT-TTF molecular orbitals, appear at low temperature (T) in the 2D conducting layers upon destabilizing the short-range-repulsion induced nonmagnetic, charge-ordered state¹⁶ with pressure^{8,17} (Fig. 1b). The high-pressure WF state is stable against pressurization so long as charge order is suppressed, where the Weyl nodes are fixed at the Fermi energy E_F due to the 3/4-filled nature of the energy band^{13,14}. The emergence of WFs next to an ordered phase is a particularly rare situation in 2D systems, suggesting that α -I₃ may be a promising platform for studying Coulomb correlation effects of WFs^{10,12,17-20}. In fact, recent static NMR spin (Knight) shift K measurements⁹ have demonstrated a logarithmic velocity enhancement induced by the long-range part of the Coulomb interaction¹² as well as a ferrimagnetic spin polarization due to the conventional short-range repulsions. In addition, the energy spectrum of α -I₃ has a remarkable duality: At lower energy near E_F , a WF regime possessing an energy-linear density of states (DOS) extends approximately up to $|E_W - E_F| \sim 12\text{meV}$ ($\sim 150\text{ K}$), while at higher energy above $|E_W - E_F|$ a conventional 2D metallic regime with a constant DOS shows up (insets of Fig. 2a)^{9,13,21}. Exploiting this dual characteristic, the WF state can be investigated in direct comparison with the conventional 2D metallic state in the same compound by varying the experimental energy scale (i.e., temperature) over $|E_W - E_F|$. That is, the conventional knowledge

of correlation studies elaborated in ordinary itinerant electron systems is to be utilized in quantitative assessments of interacting WFs.

For characterizing the strength and the nature of Coulomb correlations, the NMR spin-lattice relaxation rate divided by T , $1/T_1T$, probing the wavenumber \mathbf{q} average of the dynamic spin susceptibility $\chi(\mathbf{q}, \omega)$ (ω : frequency of MHz), provides a powerful means as has been proved in conventional correlated materials²²⁻²⁴. Figure 2a presents the temperature dependence of $1/T_1T$ and the squared Knight shift K^2 in α -I₃, where a high pressure of 2.3 GPa is applied to completely suppress charge order. The WF state is stabilized approximately below 150 K where both $1/T_1T$ and K^2 decrease with decreasing T , while a 2D metal-like state appears above 150 K showing T -independent natures for both quantities, in agreement with the aforementioned dual aspect of the DOS (insets of Fig. 2a). In conventional itinerant electron systems, the ratio of $1/T_1T$ to the square of K , $\mathcal{K} = 1/(T_1TS_0\beta K^2)$, named the Korringa ratio, measures the strength of the Coulomb correlations^{23,24}, where $S_0 = (4\pi k_B/\hbar)(\gamma_n/\gamma_e)^2$ with the electron (nuclear) gyromagnetic ratio γ_e (γ_n) and β is a form factor standing for the anisotropy of the nuclear hyperfine interaction (see **Methods**). For weak correlations, the value of \mathcal{K} is of the order of unity and does not considerably vary with temperature (the Korringa law).^{23,24} A sizable deviation of \mathcal{K} from unity would signify enhanced Coulomb correlations and characterise their nature, namely, $\mathcal{K} > (<) 1$ stands for enhanced antiferromagnetic (ferromagnetic) spin fluctuations. Above 150 K, the present results show that the Korringa law appears to hold and \mathcal{K} is ~ 3 (Fig. 2b), such as have been observed in typical 2D organic metals θ -(BEDT-TTF)₂I₃²⁵ and κ -(BEDT-TTF)₂Cu(NCS)₂²⁶, corroborating the 2D metallic picture with moderate short-range repulsions.

Contrary, below 150 K, a clear breakdown of the Korringa law sets in and an orders-of-magnitude increase of \mathcal{K} emerges: $\mathcal{K} \sim 10^3$ at 10 K (Fig. 2b). The non-interacting WFs would satisfy the Korringa law²⁷, giving rise to $\mathcal{K} \approx 1.71$ within the DOS approximation (instead of $\mathcal{K} = 1$ for ordinary free electrons). Large \mathcal{K} values are also reported in the conventional correlated materials near a Mott transition, where the growing finite- \mathbf{q} AFM fluctuations push up the \mathbf{q} average of the dynamic susceptibility $\chi(\mathbf{q}, \omega) (\propto 1/T_1T)$, while the static uniform susceptibility $\chi(\mathbf{q} \rightarrow 0, 0) (\propto K)$ remains unaffected. However, the values of \mathcal{K} are 10 or less in these systems, at the very most²². The present observation of an extraordinary size for \mathcal{K} of $\sim 10^3$ and its prominent temperature evolution clearly indicates that WFs possess a novel Coulomb-correlation mechanism distinct from the paradigm of conventional electrons governed by short-range repulsions.

For 2D WFs, one has to recall that the conduction and valence bands touch at E_F and constitute two Weyl nodes at $\pm \mathbf{k}_0$ in momentum space, around which the Coulomb interaction remains long-ranged owing to the weak metallic screening effects. The electronic excitations at low temperature exclusively appear around these nodes, which can be sorted into two processes characterized by a contrasting momentum transfer $\hbar \mathbf{q}$, C_1 ($\mathbf{q} \sim 0$) and C_2 ($\mathbf{q} \sim 2\mathbf{k}_0$) in Fig. 3c. Note that the NMR relaxation rate $1/T_1T$ probes the sum of the C_1 and C_2 processes, whereas the shift K sees only the former (C_1 : in particular $\mathbf{q} = 0$).

To evaluate the impacts of the long-range Coulomb interaction on these processes, we have performed a renormalization-group (RG) calculation at the one-loop level for dealing with the self-energy corrections, by combining the leading-order large- N approximation⁹ (**Extended Data Fig. 3**) and the general tilted Weyl Hamiltonian¹³⁻¹⁵ (for details, see **Methods**). The bare

Coulomb coupling $\alpha \approx e^2/\varepsilon\hbar v$, which is the ratio of the Coulomb potential to the electron kinetic energy, is estimated to be ≈ 8.4 by using $\varepsilon \approx 30$ and $v = 2.4 \times 10^4 \text{ m s}^{-1}$ as determined from fitting $\chi(0, 0)$ ⁹, where ε is the permittivity and v is the electron velocity. We find that the RG calculation can properly trace the observed excess suppression of K^2 beneath $1/T_1T$ (Fig. 3a) and hence the prominent increase of \mathcal{K} towards lower temperature (Fig. 3b). The sharp contrast of the temperature dependence between K^2 and $1/T_1T$ can be accounted for by the velocity renormalization that remarkably suppresses only the $\mathbf{q} = 0$ responses⁹; namely, the $\mathbf{q} = 0$ static spin susceptibility (K), probing C_1 , is directly affected by this renormalization (Fig. 3e), leading to a continuous drop of K^2 on cooling^{9,12}. On the other hand, the \mathbf{q} -summed $\chi(\mathbf{q}, \omega)$ ($1/T_1T$), probing the sum of C_1 and C_2 , is rather enhanced over the non-interacting values while the C_1 process dies off on cooling. This means that the C_2 process is not suppressed by the renormalization and becomes prevailing at low temperature (Fig 3d), causing a levelling-off of $1/T_1T$ as presented in Fig. 3a. Furthermore, the tilt of the cones is perceived to little affect these results (Fig. 3b). Thus, the RG calculation demonstrates that the observed enormous increase of \mathcal{K} is a ubiquitous nature of 2D WFs which is promoted directly by the strong Coulomb correlations.

Remarkably, however, we additionally find that $1/T_1T$ shows a sudden upturn below 3 K and increases by a factor of 2 towards the lowest measured temperature (1.7 K; Fig. 4a). This upturn cannot be reproduced by calculations incorporating either a residual finite DOS at E_F (**Extended Data Fig. 1**) or the velocity renormalization (Fig. 3a) as both of them lead not to an upturn but a levelling-off (Supporting analyses are given in the **Methods**). Here, we recall that the T -driven RG flow that we extracted from fitting the shift data⁹ reduces the Coulomb coupling α towards lower energy. However, the coupling remains rather large in the present

temperature range: $\alpha \approx 2.0$ at $T = 5$ K (**Extended Data Fig. 2**). Considering this sizeable value for α , our observation of the upturn in $1/T_1T$ may signify an incipient instability of nodal fermions relevant to the Coulomb correlations.

For 2D WFs with a vanishing DOS at E_F , theoretical studies have suggested excitonic pairing instabilities²⁸ for a finite value of α which, above a critical value $\alpha_c \sim 1$, lead to a dynamic fermion mass generation^{2,5,6} – the counterpart of chiral symmetry breaking in the quantum electrodynamics^{3,4}. By analogy, this instability has widely been analysed within the framework of the excitonic mass-gap (or Schwinger-Dyson) equation^{2,5,6}. In contrast to the Bardeen-Cooper-Schrieffer (BCS) theory describing superconductivity, eight different types of gap possessing strong momentum dependence are conceivable, which can be categorised in terms of the time-reversal and inversion symmetries in addition to the total momentum⁶ (see **Supplementary Information** and **Extended Data Table 1**). Given that a spin-triplet pairing can cause magnetic fluctuations, the observed upturn of $1/T_1T$ likely pertains to the onset of a spin-triplet excitonic fluctuation.

To investigate this hypothesis, we have calculated $1/T_1T$, using the ladder approximation and evaluating the excitonic gap function at a linearized level with the velocity renormalization taken into account (see **Methods** and **Extended Data Figs. 4,5**). For finite values of α approximately larger than unity, we confirm the appearance of an upturn in the calculated $1/T_1T$ as a clear manifestation of the growing excitonic fluctuations (Fig. 4b), which sets in at a similar temperature as in the experimental data (Fig. 4a). Further examination of the gap properties reveal that the emergent fluctuations refer to a spin-triplet, even-parity excitonic pairing with

respect to the C_2 process in Fig. 3c. These calculations thus indicate that the observation of the $1/T_1T$ upturn marks a precursor of excitonic condensation.

Khveshchenko⁶ has recently estimated the ratio of the mean-field critical temperature T_C to the excitonic gap Δ for 2D WFs, and by omitting the velocity renormalization, arrived on the expressions

$$\frac{T_C}{\Delta} \approx \frac{1}{|\ln(1 - \tilde{\alpha}_C/\tilde{\alpha})|}, \quad (1)$$

$$\Delta = v\Lambda \exp\left(-\frac{2\pi - 4\arctan\sqrt{2\tilde{\alpha} - 1}}{\sqrt{2\tilde{\alpha} - 1}}\right), \quad (2)$$

where $\tilde{\alpha} = \alpha/(1 + N\pi\alpha/8\sqrt{2})$ with $N = 4$, coming from the two spin projections and two nodes, $\tilde{\alpha}_C = 0.5$ and Λ is a momentum cutoff of the inverse lattice constant. For α -I₃ having a large bare Coulomb coupling ($\alpha \approx 8.4$), the estimated critical temperature and the gap are rather large, $T_C \sim \Delta \sim 10$ K, and remain finite (of ~ 40 mK) even if the RG flow is taken into account ($\alpha \approx 2.0 > \alpha_C$ at the lowest T) (see **Methods**). This is consistent with our observation where the incipient excitonic fluctuations appear to develop from higher temperatures towards T_C . Furthermore, previous reports of an in-plane insulating behaviour in α -I₃ at a similar temperature^{17,29} may provide another sign of the precursor of condensation³⁰, in line with our results.

Thus, our NMR experiment and corresponding theoretical calculations unveil the extraordinary Coulomb correlation effects that are characteristic of relativistic massless electrons subjected to a considerable long-range Coulomb interaction. This work paves a novel way to

explore the rich interaction physics of “strongly correlated Weyl fermions”² that has been so-far discussed only theoretically in a solid-state platform.

References

1. Wehling, T. O., Black-Schaffer, A. M. & Balatsky, A. V. Dirac materials. *Adv. Phys.* **63**, 1–76 (2014).
2. Kotov, V. N., Uchoa, B., Pereira, V. M., Guinea, F. & Castro Neto, A. H. Electron-electron interactions in graphene: current status and perspectives. *Rev. Mod. Phys.* **84**, 1067 (2012).
3. Pisarski, R. D. Chiral-symmetry breaking in three-dimensional electrodynamics. *Phys. Rev. D* **29**, 2423(R) (1984).
4. Applequist, T. W., Bowick, M., Karabali, D. & Wijewardhana, L. C. R. Spontaneous chiral-symmetry breaking in three-dimensional QED. *Phys. Rev. D* **33**, 3704 (1986).
5. Khveshchenko, D. V. Ghost Excitonic Insulator Transition in Layered Graphite. *Phys. Rev. Lett.* **87**, 246802 (2001).
6. Khveshchenko, D. V. Massive Dirac fermions in single-layer graphene. *J. Phys. Condens. Matter* **21**, 075303 (2009).
7. Wei, H., Chao, S.-P., & Aji, V. Excitonic Phases from Weyl Semimetals. *Phys. Rev. Lett.* **109**, 196403 (2012).
8. Kajita, K., Nishio, Y., Tajima, N., Suzumura, Y. & Kobayashi, A. Molecular Dirac Fermion systems—theoretical and experimental approaches. *J. Phys. Soc. Jpn.* **83**, 072002 (2014).
9. Hirata, M. et al. Observation of an anisotropic Dirac cone reshaping and ferrimagnetic spin polarization in an organic conductor. *Nat. Commun.* **7**, 12666 (2016).
10. Isobe, H. & Nagaosa, N. Coulomb Interaction Effect in Weyl Fermions with Tilted Energy

- Dispersion in Two Dimensions. *Phys. Rev. Lett.* **116**, 116803 (2016).
11. Yasuoka, H., et al. Emergent Weyl fermion excitations in TaP explored by 181-Ta quadrupole resonance. arXiv:1611.07311 (2016).
 12. Isobe, H. & Nagaosa, N. N. Renormalization effects on quasi-two-dimensional organic conductor α -(BEDT-TTF)₂I₃. *J. Phys. Soc. Jpn.* **81**, 113704 (2012).
 13. Katayama, S., Kobayashi, A. & Suzumura, Y. Pressure-induced zero-gap semiconducting state in organic conductor α -(BEDT-TTF)₂I₃ salt. *J. Phys. Soc. Jpn.* **75**, 054705 (2006).
 14. Kobayashi, A., Katayama, S., Suzumura, Y. & Fukuyama, H. Massless Fermions in organic conductors. *J. Phys. Soc. Jpn.* **76**, 034711 (2007).
 15. Goerbig, M. O., Fuchs, J.-N., Montambaux, G. & Piéchon, F. Tilted anisotropic Dirac cones in quinoid-type graphene and α -(BEDT-TTF)₂I₃. *Phys. Rev. B* **78**, 045415 (2008).
 16. Ishikawa, K. et al. Spin excitations in the quasi-two-dimensional charge-ordered insulator α -(BEDT-TTF)₂I₃ probed via ¹³C NMR. *Phys. Rev. B* **96**, 085154 (2016).
 17. Liu, D. et al. Insulating Nature of Strongly Correlated Massless Dirac Fermions in an Organic Crystal. *Phys. Rev. Lett.* **116**, 226401 (2016).
 18. Kobayashi, A., Suzumura, Y., Fukuyama, H. & Goerbig, M. O. Tilted-Coneinduced easy-plane pseudo-spin ferromagnet and Kosterlitz–Thouless transition in massless Dirac fermions. *J. Phys. Soc. Jpn.* **78**, 114711 (2009).
 19. Tanaka, Y. & Ogata, M. Correlation Effects on Charge Order and Zero-Gap State in the Organic Conductor α -(BEDT-TTF)₂I₃. *J. Phys. Soc. Jpn.* **85**, 104706 (2016).
 20. Matsuno, G. & Kobayashi, A. Effect of Interband Fluctuation on Spin Susceptibility in Molecular Dirac Fermion System α -(BEDT-TTF)₂I₃. *J. Phys. Soc. Jpn.* **86**, 014705 (2017).
 21. Kino, H. & Miyazaki, T. First-principles study of electronic structure in α -(BEDT-TTF)₂I₃ at ambient pressure and with uniaxial strain. *J. Phys. Soc. Jpn.* **75**, 034704 (2006).

22. Bulut, N., Hone, D., Scalapino, D. J. & Bickers, N. E. Random-phase-approximation analysis of NMR and neutron-scattering experiments on layered cuprates. *Phys. Rev. Lett.* **64**, 2723-2726 (1990).
23. Moriya, T. The Effect of Electron-Electron Interaction on the Nuclear Spin Relaxation in Metals. *J. Phys. Soc. Jpn.* **18**, 516-520 (1963).
24. Narath, A. & Weaver, H. T. Effects of Electron-Electron Interactions on Nuclear Spin-Lattice Relaxation Rates and Knight Shifts in Alkali and Noble Metals. *Phys. Rev.* **175**, 373-382 (1968).
25. Hirata, M., Miyagawa, K., Kanoda, K. & Tamura, M. Electron correlations in the quasi-two-dimensional organic conductor θ -(BEDT-TTF)₂I₃ investigated by ¹³C NMR. *Phys. Rev. B* **85**, 195146 (2012).
26. Itaya, M., Eto, Y. & Kawamoto, A. Antiferromagnetic Fluctuations in the Organic Superconductor κ -(BEDT-TTF)₂Cu(NCS)₂ under Pressure. *Phys. Rev. Lett.* **102**, 227003 (2009).
27. Dóra, B. & Simon, F. Unusual hyperfine interaction of Dirac electrons and NMR spectroscopy in graphene. *Phys. Rev. Lett.* **102**, 197602 (2009).
28. Keldysh, L. V. & Kopaev, Y. V. Possible instability of the semimetallic state toward Coulomb interaction. *Sov. Phys. Solid State* **6**, 2219 (1965).
29. Tajima, N., Kato, R., Sugawara, S., Nishio, Y. & Kajita, K. Interband effects of magnetic field on Hall conductivity in the multi-layered massless Dirac fermion system α -(BEDT-TTF)₂I₃. *Phys. Rev. B* **85**, 033401 (2012).
30. Béal-Mond, M. T., Maki, K. & Fukuyama, H. Effects of the Excitonic Fluctuations Above the Transition Temperature. *J. Low Temp. Phys.* **112**, 73 (1972).

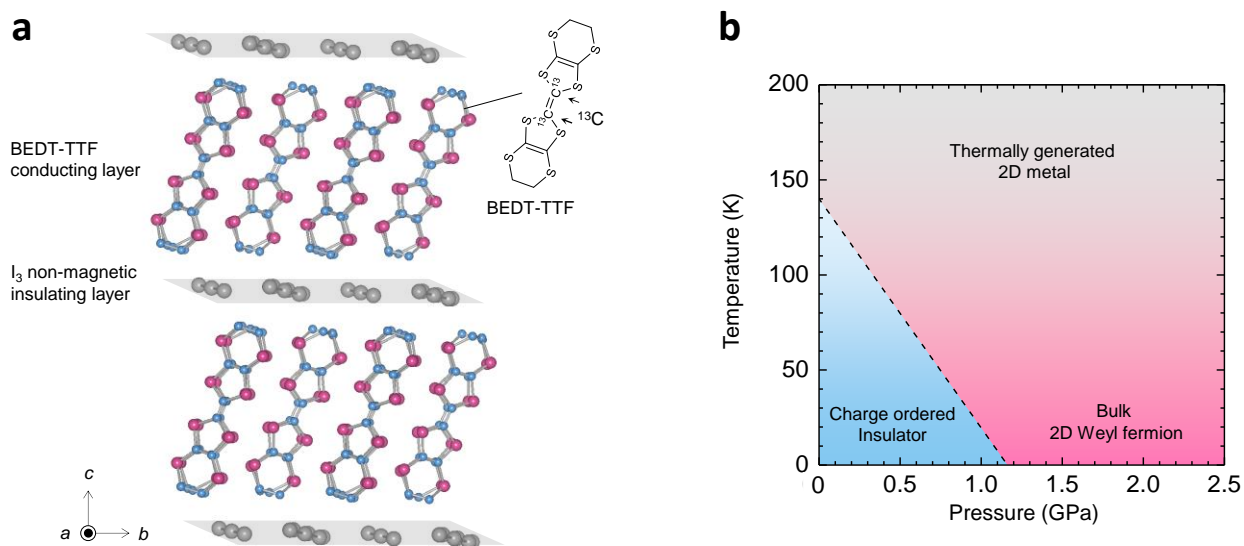


Figure 1 | Crystal structure and phase diagram of α -(BEDT-TTF)₂I₃. **a**, Side view of the crystal structure of α -(BEDT-TTF)₂I₃. The conducting BEDT-TTF layers are separated by non-magnetic insulating layers of I₃. Inset: BEDT-TTF molecular structure with selectively introduced ¹³C isotopes indicated by arrows. **b**, Pressure-temperature phase diagram of α -(BEDT-TTF)₂I₃ taken from Ref. 9. The dashed line indicates the first-order transition line.

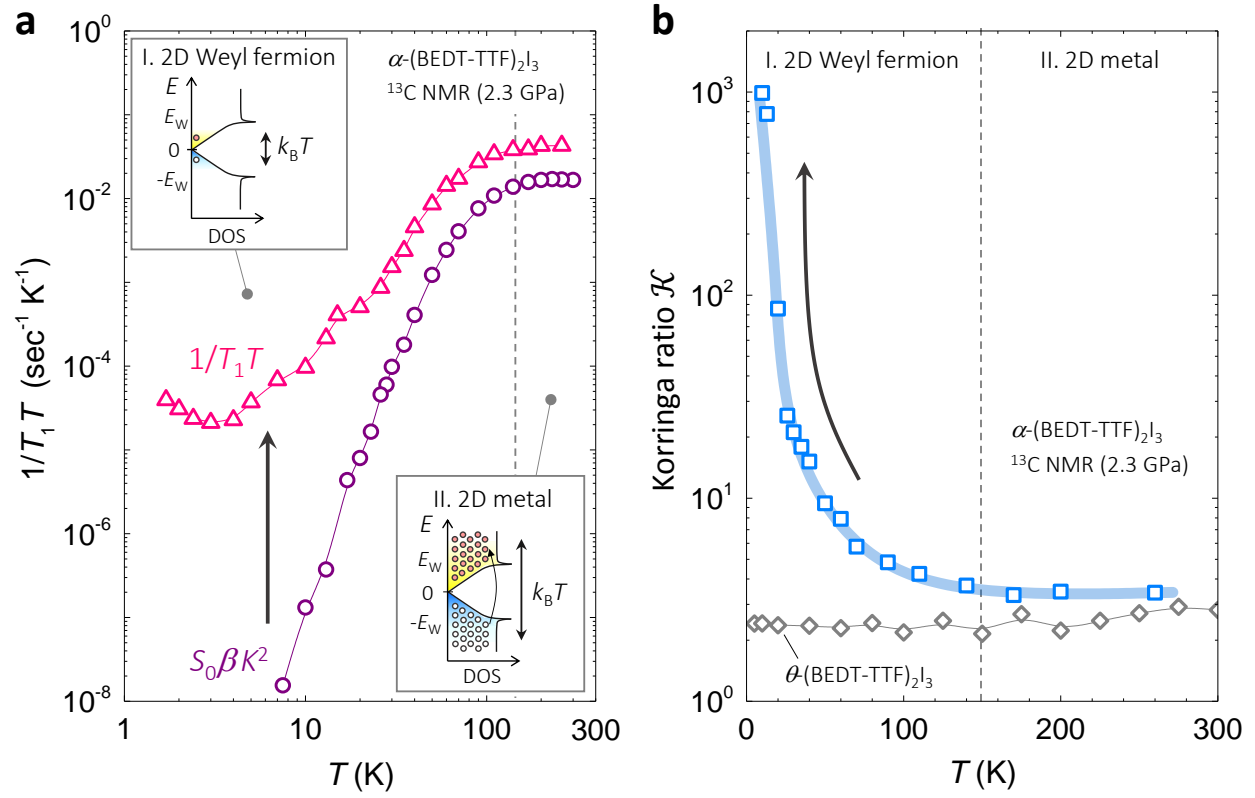


Figure 2 | Enormous Coulomb correlations of 2D WFs in $\alpha\text{-(BEDT-TTF)}_2\text{I}_3$. **a**, Temperature dependence of the ^{13}C -NMR spin-lattice relaxation rate $1/T_1T$ (triangles) and the Knight shift squared K^2 (circles) measured at a pressure of 2.3 GPa and a magnetic field of 6 T, using the ^{13}C nuclei at the centre of BEDT-TTF molecules (inset of Fig. 1). Inset: The DOS profile near $E_F (= 0)$ with thermally generated electron-hole pairs (circles) indicated for low (I) and high (II) temperatures, respectively. The DOS is linear up to $|E_W - E_F|$ and levels off above it. **b**, Temperature dependence of the ^{13}C -NMR Korrington ratio \mathcal{K} (squares). The results for the 2D organic metal $\theta\text{-(BEDT-TTF)}_2\text{I}_3$ (diamonds) is plotted as a reference²⁵ (for details, see **Methods**).

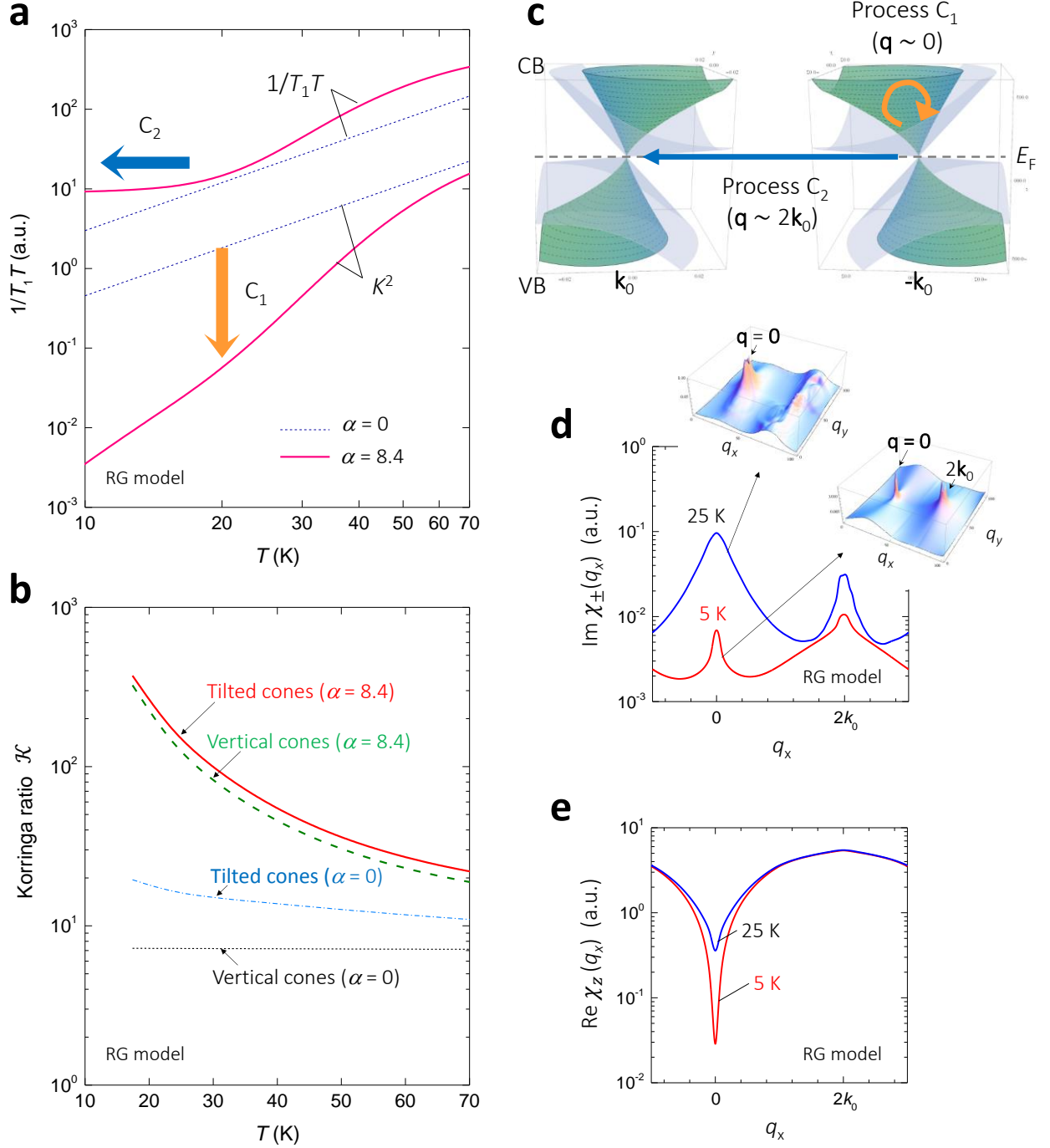


Figure 3 | Simulations based on the RG approach. **a**, Calculated temperature dependence of $1/T_1 T$ and K^2 for double tilted Weyl cones with the velocity renormalization due to the self-energy correction considered using the RG technique within the leading-order large- N expansion⁹. The Coulomb coupling is chosen as $\alpha = 0$ (dashed) and 8.4 (solid) determined from

fitting the K data⁹ (see **Methods**). **b**, Calculated Korringa ratio \mathcal{K} as a function of temperature for double cones with and without the tilt and self-energy correction: black dotted, vertical cones ($\alpha = 0$); blue dash-dotted, tilted cones ($\alpha = 0$); green dashed, vertical cones ($\alpha = 8.4$); red solid, tilted cones ($\alpha = 8.4$). **c**, Double tilted Weyl cones in a -I₃ for $\alpha = 0$ (grey cones) and 8.4 (green reshaped cones). Two Weyl nodes appear at $\pm \mathbf{k}_0$ where the conduction band (CB) and the valence band (VB) touch at E_F . Relevant excitation processes at low temperature (C_1 and C_2) are indicated by arrows. **d,e**, Calculated wavevector dependence of the transverse (χ_{\pm}) and longitudinal (χ_z) spin susceptibilities for double tilted cones with the self-energy correction ($\alpha = 8.4$). The direction of q_x is set along the line connecting two nodes. The calculated profiles of $\text{Im}\chi_{\pm}$ (**d**) and $\text{Re}\chi_z$ (**e**) at 25 K (blue) and 5 K (red) are presented. Inset of **d**: corresponding 3D plot of $\text{Im}\chi_{\pm}$ on the q_x - q_y plane. Note that the $q_x = 0$ term in $\text{Re}\chi_z$ corresponds to the Knight shift K , while the \mathbf{q} -summation of $\text{Im}\chi_{\pm}$ amounts to $1/T_1T$. a.u. stands for the arbitrary units.

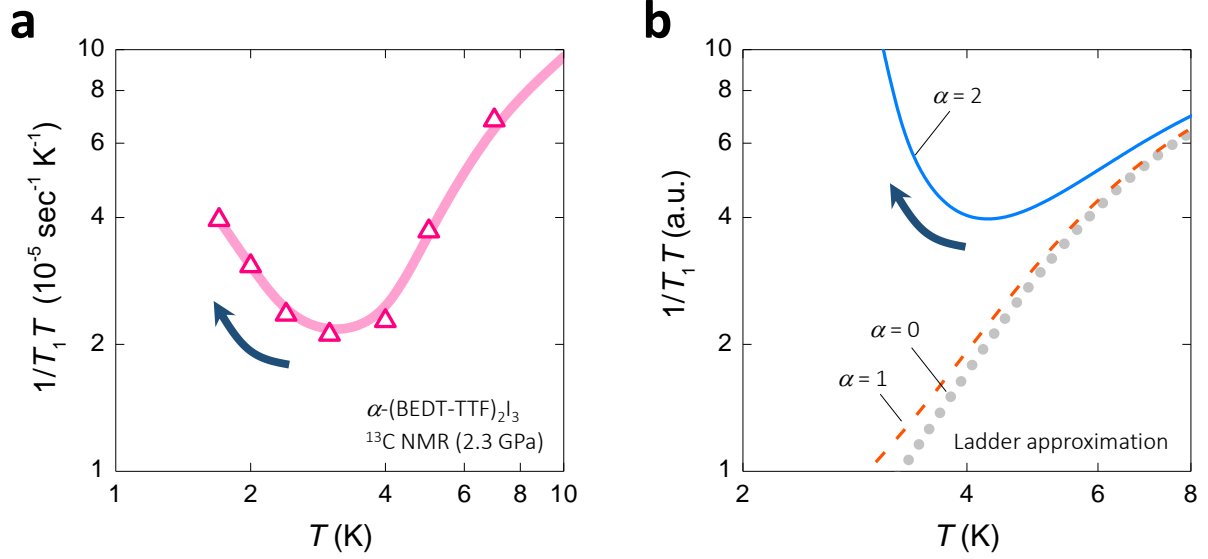


Figure 4 | Incipient excitonic fluctuations. **a**, The low-temperature close up of $1/T_1 T$ in Fig. 2a. **b**, Calculated temperature dependence of $1/T_1 T$ based on the ladder approximation at a linearized level for the gap with the velocity renormalization taken into account. The Coulomb coupling of $\alpha = 0$ (grey dotted), 1 (orange dashed) and 2 (blue solid) is used in the calculation (see **Methods**).

Methods

Experimental backgrounds. High-quality single crystals of α -(BEDT-TTF)₂I₃ (α -I₃) were prepared using conventional methods. Initially, the double-bond connected central carbon atoms in BEDT-TTF molecules were selectively replaced by carbon-13 (¹³C) isotopes with a nuclear spin-1/2 by 99% (upper inset of Fig. 1a). Single crystals were synthesized from the ¹³C-enriched BEDT-TTF molecules by electrochemical technique (the same crystals used as in Ref. 9.). A hydrostatic pressure of 2.3 GPa was applied to the sample using a BeCu/NiCrAl clamp-type pressure cell (C&T Factory) and Daphne 7373 oil (Idemitsu), following the thermal treatments described in Ref. 9. A static magnetic field H of 6 T was applied parallel to the 2D conducting plane ($H||ab$). NMR measurements at ¹³C nuclei were performed using a commercially available homodyne spectrometer by means of the standard spin-echo technique, with the echo signals recorded at a fixed radiofrequency and converted to NMR spectra via Fourier transformation. The measurements of the ¹³C spin-lattice relaxation time T_1 were obtained from the standard single-exponential fits to the recovery of the nuclear magnetization after saturation.

The observed ¹³C-NMR spectra are composed of eight lines, the assignment of which can be properly done from the knowledge of the crystal structure as described elsewhere.^{9,31,32} The eight lines can be assigned to three non-equivalent molecular sites in the 2D unit cell, A (= A'), B and C.³³

The total NMR shift, S , for a given molecular site is defined as the centre-of-mass position of the ¹³C lines arising from the corresponding molecule, which is a sum of the spin shift (Knight shift) K and the temperature-independent chemical shift σ ($S = K + \sigma$) with little contributions from the orbital term³⁴. The chemical shift σ is determined from the field-angle

dependence of the total shift at 3 K where the spin shift is expected to be vanishingly small as we discussed previously (see Ref. 9) and thus one can assume $S(3 \text{ K}) \approx \sigma(3 \text{ K})$. Subtracting σ , the total shift S is eventually converted to the Knight shift K .

The spin-lattice relaxation rate divided by temperature, $1/T_1T$, was measured for each molecule at respective lines, which is related to the imaginary part of the transverse spin susceptibility as follows^{23,24}

$$\frac{1}{T_1T} = \frac{2\gamma_n^2 k_B (\bar{A}_\perp)^2}{g^2 \mu_B^2} \sum_{\mathbf{q}} \frac{\text{Im}\chi_\perp(\mathbf{q}, \omega_0)}{\omega_0}, \quad (3)$$

where \mathbf{q} is the wavenumber vector, \bar{A}_\perp is the transverse component of the mean hyperfine coupling tensor averaged for the two central ^{13}C nuclei in a molecule (inset of Fig. 1a) and ω_0 is the resonance frequency used in the NMR experiments ($\approx 64 \text{ MHz}$ for the present case).

The evaluation of the Coulomb correlations is done using the values of K and $1/T_1T$ at the molecule A ($= A'$), where the excitations around the Weyl nodes on E_F are probed most uniformly in momentum space^{9,35}. Since the Knight shift in this compound has a large anisotropy due to the anisotropic hyperfine interaction at the ^{13}C nuclei^{32,36,37}, all measurements are performed in a magnetic field applied 60° off the crystalline a axis, where the modulus of the Knight shift at the molecule A ($= A'$) becomes maximum. (Note that this configuration is identical to one of those used in Ref. 9). For the sake of simplicity, we omit the site index throughout this study. (When the index is needed, it will be specifically mentioned.)

The Korringa relation^{23,24,32,34,38} is given by the following expression

$$\frac{1}{T_1 T K^2} = \frac{4\pi k_B}{\hbar} \left(\frac{\gamma_n}{\gamma_e} \right)^2 \beta(\zeta, \eta) \mathcal{K}, \quad (4)$$

where γ_n (γ_e) is the nuclear (electron) gyromagnetic ratio, \mathcal{K} is the Korringa ratio and

$$\begin{aligned} \beta(\zeta, \eta) &= \left(\frac{\bar{A}_\perp}{\bar{A}_\parallel} \right)^2 \\ &= \frac{(\bar{A}^{xx} / \bar{A}^{zz})^2 (\sin^2 \eta + \cos^2 \zeta \cos^2 \eta) + (\bar{A}^{yy} / \bar{A}^{zz})^2 (\cos^2 \eta + \cos^2 \zeta \sin^2 \eta) + \sin^2 \zeta}{\{(\bar{A}^{xx} / \bar{A}^{zz})^2 \sin^2 \zeta \cos^2 \eta + (\bar{A}^{yy} / \bar{A}^{zz})^2 \sin^2 \zeta \sin^2 \eta + \cos^2 \zeta\}^2} \end{aligned} \quad (5)$$

is the form factor describing the anisotropy of the hyperfine coupling (the ratio of the transverse component \bar{A}_\perp to the longitudinal one \bar{A}_\parallel).^{32,34} Here, $\mathcal{A} = (\bar{A}^{xx}, \bar{A}^{yy}, \bar{A}^{zz})$ are the principle components of the averaged hyperfine coupling tensor in the molecule A (= A'), and (ζ, η) stand for the polar and azimuthal angles in the principal coordinate of BEDT-TTF molecules (for details, see Refs 32 and 34). For the evaluation of \mathcal{K} , we used the principle values determined at ambient pressure around room temperature³² as the pressure and temperature dependence of \mathcal{A} is negligibly small,⁹ which leads to $\beta \sim 0.46$ for the current field geometry by using the X-ray crystal structure data determined at close pressure.³⁹

Simulations based on the DOS approximations for the non-interacting 2D WFs. For an isolated 2D Weyl cone with electron-hole symmetry and a vanishing DOS at E_F , the temperature dependence of the NMR spin-lattice relaxation rate $1/T_1$ and the Knight shift K are expressed by a simple power law for the non-interacting DOS approximation: $1/T_1 \propto T^3$ and $K \propto T$.^{27,35} This expression is, however, only valid for a weak field (H) limit, where the electron Zeeman energy ($E_Z = g\mu_B H$) is much smaller than the thermal energy ($k_B T$). At 6 T, for example, the Zeeman term corresponds to $E_Z/k_B \approx 8$ K (for $g = 2$), indicating that the low-field limit might be invalid below 8 K, where the Zeeman-induced finite DOS at E_F should be involved. Furthermore, previous Hall measurements in pressurized α -I₃ suggests a small shift of E_F from the band-crossing point (set as $E = 0$) of the size $E_F/k_B \lesssim 1.5$ K probably by a self-doping effect due to small sample imperfection,^{29,40} which generates a finite Fermi surface and thus a finite DOS at E_F . Both cases in turn lead to a levelling-off of $1/T_1 T$ and K at low temperature as in conventional 2D metals.^{41,42}

To investigate the influence of these effects, we have calculated the chemical potential μ and H dependence of K and $1/T_1 T$ in the non-interacting DOS approximation using the canonical expressions of $K \sim -\partial/\partial H \int_{-\infty}^{\infty} dE [D_+(E)f(E) - D_-f(E)]$ and $1/T_1 \sim \int_{-\infty}^{\infty} dE D_+(E)f(E) \int_{-\infty}^{\infty} dE' D_-(E')\{1 - f(E')\}\delta(E - E')$ ^{41,42} valid for an arbitrary field strength, where $D_{\pm}(E) = D(E \mp E_Z/2)/2$ is the electron DOS for up/down (+/-) spin, $f(E) = 1/[1 + \exp\{(E - \mu)/k_B T\}]$ is the Fermi distribution function and $\delta(E)$ is the Dirac delta function. The calculated traces of K and $1/T_1 T$ are depicted in **Extended Data Figure 1**. We find that the aforementioned amount of self doping eventually little affects the results in our experimental temperature range ($T \geq 1.7$ K). For $\mu = 0$ with decreasing temperature, K shows a monotonic crossover from $K \propto T$ to $K = \text{const.}$, whereas $1/T_1 T$ switches from $1/T_1 T \propto T^2$ to

$1/T_1T = \text{const.}$ with a minimum at $T_{\min} \approx E_Z/5k_B$. For 6 T, this amounts to $T_{\min} \approx 1.6$ K. These calculations thus indicate that the low-field approximation with $\mu = 0$ is valid within the present experimental conditions ($T \geq 1.7$ K and $H = 6$ T), demonstrating that the influence of the residual DOS at E_F upon the profile of $1/T_1T$ can be ruled out.

Renormalization-group calculation based on the tilted Weyl Hamiltonian. Because α -I₃ has a very low-symmetry crystal containing only the inversion symmetry,^{33,39,43} the 2D tilted Weyl cones appear by an accidental degeneracy^{44,45} at \mathbf{k}_0 and $-\mathbf{k}_0$ ^{13-15,21,46-48} which are shown to be robust against perturbations like modulations of transfer integrals in a finite range due to the 3/4-filled nature of the electronic band.^{13,35,49-54} The Weyl fermion state is indeed confirmed by a range of experiments such as transport,^{17,55-63} calorimetric,^{64,65} optical^{66,67} and nuclear magnetic resonance^{9,31,37} measurements. The low-energy effective model for 2D WFs is described by the tilted Weyl Hamiltonian¹³⁻¹⁵ based on the Luttinger-Kohn (LK) representation⁶⁸ and molecular orbitals, which is given by

$$H = \hbar \sum_{i=x,y} (w_i + v_i \hat{\sigma}_i) k_i, \quad (6)$$

where $\hat{\sigma}_x$ and $\hat{\sigma}_y$ are the Pauli matrices; $\mathbf{w} = (w_x, w_y)$ and $\mathbf{v} = (v_x, v_y)$ are velocities describing the tilt and the anisotropy of 2D Weyl cones, respectively; and $\mathbf{k} = (k_x, k_y)$ is the wavenumber vector measure from the node \mathbf{k}_0 . (For the tilted Weyl Hamiltonian, see **Supplementary Discussion C.**) Here, for the sake of simplicity, we don't distinguish the two nodes at $\pm\mathbf{k}_0$ and concentrate on the one at \mathbf{k}_0 , while in the next section we shall specifically distinguish them.

To deal with the long-range Coulomb interaction, we have considered the self-energy correction effect in the framework of the one-loop order renormalization-group (RG) calculation in the leading order in $1/N$ ($N \gg 1$) with $N = 4$ being the number of fermion species (two spin projections and two nodes). The employed diagrams are summarized in **Extended Data Fig.3**. The details are described in Ref. 9 (the RG equations are given in Eq. 2 therein). (Note that the vertex corrections are automatically taken into account when the RG equations are solved, while they are not used in the derivation of the RG equations.) In the present work, we use the resultant upward flow of the velocity \mathbf{v} (\mathbf{w} does not flow at the one-loop level) due to the running coupling constant^{2,12,69-71} that is determined from fitting the temperature dependence of the uniform spin susceptibility (Knight shift).⁹ Briefly, we assumed four velocities $\mathbf{w} = u\mathbf{w}^{\text{TB}}$ and $\mathbf{v} = u\mathbf{v}^{\text{TB}}$ as the initial velocity at the momentum cutoff Λ ($= 0.667 \text{ \AA}^{-1}$: of the size of the inverse lattice constant)³⁹ and a phenomenological parameter $u \approx 0.35$ (representing the bandwidth renormalization effect) determined from the fit. $\mathbf{w}^{\text{TB}} = (-5.06, 0.750)$ and $\mathbf{v}^{\text{TB}} = (6.70, 6.86)$ (in 10^4 m s^{-1}) are velocities given by the effective tight-binding calculation for $\alpha\text{-I}_3$ ³⁵ as discussed previously (see Ref. 9 and the supplementary materials therein for details of the fitting analyses).

The dimensionless Coulomb coupling, which is the ratio of the Coulomb potential to the electron kinetic energy, is given by $\alpha = e^2 / \left(\epsilon \hbar \sqrt{v_x^2 \sin^2 \varphi + v_y^2 \cos^2 \varphi} \right)$ for the anisotropic 2D WFs,⁹ where ϵ is the dielectric constant and φ is an angle measured around the node at \mathbf{k}_0 . As a consequence of the T -driven renormalization, the Coulomb coupling α flows to a smaller value,^{12,14,70,71} causing a remarkable reshaping of tilted Weyl cones as depicted in Fig. 3c.⁹

Concerning the interaction, it is worthwhile to mention that the Coulomb correlations would be quite large in $\alpha\text{-I}_3$ as the WF state emerges next to a charge-ordered insulator^{19,49,72-74}

on the P - T phase diagram (Fig. 1b).^{17,57,67,75,76} Indeed, the bare Coulomb coupling constant, approximated as $\alpha \approx e^2/\varepsilon\hbar v$ due to the small anisotropy ($v_x \approx v_y \equiv v$),^{9,35} is estimated to be $\alpha \approx 8.4$ at the momentum cutoff $q = \Lambda$, (circular around the node), by employing $\varepsilon \approx 30$ and $v = 2.4 \times 10^4 \text{ m s}^{-1}$ determined from the fitting.⁹ We have calculated the flow of α as a function of energy measured from E_F for the gentle and steep slopes of the 2D tilted Weyl cone, as depicted in **Extended Data Figure 2**. The value of α has distinct values in two slopes at higher energies, while the difference becomes smaller towards lower energy and is eventually negligibly small at the low-energy limit. This is equivalent to say that the tilted cone becomes more isotropic at low energy due to the flow-induced cone reshaping, as discussed previously.⁹

Simulations based on the double 2D Weyl cones with interactions. To deal with the interacting 2D WFs with $N = 4$, we describe the WF states with an 8-component creation operator $\Psi_{\mathbf{k}}^\dagger = (c_{\mathbf{k},s,\eta}^\nu)^\dagger$, where the superscript, the second and third indices of the subscript stand for the two LK bases ($\nu = a, b$),⁶⁸ spin ($s = 1(\uparrow), -1(\downarrow)$) and node ($\eta = 1(R), -1(L)$), respectively. (For the LK representation, see **Supplementary Discussion C**.) Note that the wavenumber vector is given around the node by $\mathbf{k} = \tilde{\mathbf{k}} \mp \tilde{\mathbf{k}}_0$, where $\tilde{\mathbf{k}}$ and $\tilde{\mathbf{k}}_0$ are defined in the first Brillouin zone, and the two Weyl nodes locate at $\pm \tilde{\mathbf{k}}_0$. The effective 8×8 Hamiltonian describing interacting 2D WFs then reads

$$H_{\text{eff}} = \sum_{\mathbf{k}} \Psi_{\mathbf{k}}^\dagger H_0 \Psi_{\mathbf{k}} + \sum_{\mathbf{q}} V_0(\mathbf{q}) \rho(\mathbf{q}) \rho(-\mathbf{q}), \quad (7)$$

where

$$H_0 = \hbar(\mathbf{w} \cdot \mathbf{k} \hat{\sigma}_0 \otimes \hat{\tau}_z + v_x k_x \hat{\sigma}_x \otimes \hat{\tau}_z + v_y k_y \hat{\sigma}_y \otimes \hat{\tau}_0) \otimes \hat{s}_0 - \mu_B H \hat{\sigma}_0 \otimes \hat{\tau}_0 \otimes \hat{s}_z \quad (8)$$

is the tilted Weyl Hamiltonian^{14,15} with the spin and node-pseudospin as well as the in-plane magnetic field H included, $V_0(\mathbf{q}) = 2\pi e^2/\epsilon|\mathbf{q}|$ is the long-range Coulomb potential and $\rho(\mathbf{q}) = \sum_{\mathbf{k}} \sum_{v,s,\eta} c_{\mathbf{k},s,\eta}^{v\dagger} c_{\mathbf{k}+\mathbf{q},s,\eta}^v$ is the density operator. The Pauli matrices $\hat{\sigma}_i$, $\hat{\tau}_j$ and \hat{s}_t represent the LK pseudospin, node-pseudospin and real spin, respectively, with the three indices taking one of the four possible values ($i, j, t = 0, x, y, z$). The index 0 stands for 2×2 unit matrices. In the following, we omit the backscattering and Umklapp processes, assuming that both \mathbf{k} and $\mathbf{k} \pm \mathbf{q}$ are restricted to the vicinity of a same node. Hereafter, we thus redefine \mathbf{q} such that it is a wavenumber vector much smaller compared to $2\tilde{\mathbf{k}}_0$.

Bare Green's function for the spin s and the node η represented in the LK basis is expressed by a 2×2 matrix

$$\hat{G}_{s,\eta}^{(0)}(\mathbf{k}, i\varepsilon_n) = [(i\varepsilon_n - \eta \hbar \mathbf{w} \cdot \mathbf{k} + s \mu_B H) \hat{\sigma}_0 - \eta \hbar v_x k_x \hat{\sigma}_x - \hbar v_y k_y \hat{\sigma}_y]^{-1}, \quad (9)$$

where $i\varepsilon_n$ is the fermionic Matsubara frequency. We introduce WF Green's function $\hat{G}_{s,\eta}$, in which the velocity renormalization due to the self-energy correction by the long-range Coulomb interaction is incorporated through the RG approach mentioned above (**Extended Data Figure 3**).

The Knight shift K and the NMR spin-lattice relaxation rate divided by temperature (T) $1/T_1T$ for the l th orbital (or the l th molecular site in a -I₃; namely, referring to the sites A, A', B and C in Fig. 1a) are expressed as^{35,48}

$$K_l = \sum_{\eta, m} \text{Re}[\chi_{\eta\eta, lm}^z(\mathbf{q} = \mathbf{0}, i\omega = 0)], \quad (10)$$

$$\left(\frac{1}{T_1T}\right)_l = \sum_{\mathbf{q}, \eta, \eta'} \text{Im}[\chi_{\eta\eta', ll}^\pm(\mathbf{q}, \omega_0 + i0^+)]/\omega_0, \quad (11)$$

where ω_0 is the NMR resonance frequency. The longitudinal uniform spin susceptibility χ_{lm}^z and the transverse local spin susceptibility $\chi_{\eta, \eta', l}^\pm$ are defined by the following expressions:

$$\chi_{\eta\eta, lm}^z(\mathbf{q}, i\omega_m) = -\frac{T}{2N_L} \sum_{\substack{\mathbf{k}, n, s \\ \nu_1 \nu_2 \nu_3 \nu_4}} \mathcal{F}_{\nu_1 \nu_2 \nu_3 \nu_4}^{\eta\eta, lm} \hat{G}_{s, \eta}(\mathbf{k} + \mathbf{q}, i\varepsilon_n + i\omega_m) \hat{G}_{s, \eta}(\mathbf{k}, i\varepsilon_n), \quad (12)$$

$$\chi_{\eta\eta', ll}^\pm(\mathbf{q}, i\omega_m) = -\frac{T}{N_L} \sum_{\substack{\mathbf{k}, n \\ \nu_1 \nu_2 \nu_3 \nu_4}} \mathcal{F}_{\nu_1 \nu_2 \nu_3 \nu_4}^{\eta\eta', ll} G_{\uparrow, \eta}^{\nu_1 \nu_2}(\mathbf{k} + \mathbf{q}, i\varepsilon_n + i\omega_m) G_{\downarrow, \eta'}^{\nu_3 \nu_4}(\mathbf{k}, i\varepsilon_n). \quad (13)$$

Here, ω_m is the bosonic Matsubara frequency, N_L is the number of unitcells and \mathcal{F} is a form factor defined in the **Supplemental Discussion C**. Notably, $(1/T_1T)_l$ includes both the intra-node, $\eta = \eta'$, and inter-node, $\eta \neq \eta'$, scatterings (corresponding to the C₁ and C₂ processes in Fig. 3c, respectively), whereas K_l probes only the intra-node ones (C₁). Employing the RG correction effects evaluated from fitting the experimental Knight shift data at the site A in a -I₃ (hereafter A is not distinguished from A'),⁹ we have calculated the temperature dependence of K_A and $(1/T_1T)_A$ in terms of Eqs. 10-13 for the non-interacting ($\alpha = 0$) and interacting ($\alpha \approx 8.4$)

cases, as depicted in Fig. 3a. For each of these results, the Korringa ratio at the site A, $\mathcal{K}_A = (1/T_1TK^2)_A$, has been evaluated by assuming vertical cones (without a tilt; $\mathbf{w} = \mathbf{0}$) and tilted cones ($\mathbf{w} \neq \mathbf{0}$) (Fig. 3b). The calculated profiles of the corresponding susceptibilities in the first Brillouin zone are presented in Figs 3d and 3e at high (25 K) and low (5 K) temperatures.

Regarding the excitonic instability,^{5,6,28,77-82} the whole eight types of excitonic order parameters that generate a mass in 2D WF systems⁶ (see **Extended Data Table 1** and **Supplemental Discussion A**) are examined at a mean-field level with the aforementioned RG correction effects incorporated. We find that the even-parity excitonic pairings in the inter-node (C_2) process, such as $\langle c_R^{a\dagger} c_L^b \rangle$, give the dominant contributions towards reproducing the observed $1/T_1T$ upturn (Fig. 4a), which are described by an operator $\Phi^{2\mathbf{k}_0,e}(\mathbf{k}; \mathbf{q}) = \Psi_{\mathbf{k}+\mathbf{q}}^\dagger (\hat{\sigma}_x \otimes \hat{t}_x \otimes \hat{s}_j) \Psi_{\mathbf{k}}$ in the matrix representation. In particular, the linearized gap equation for the order parameter reads

$$\lambda \Delta_{\mathbf{k}} = \sum_{\mathbf{k}'} V_0(\mathbf{k} - \mathbf{k}') \Delta_{\mathbf{k}'} \chi^{2\mathbf{k}_0,e}(\mathbf{k}'; \mathbf{q} = \mathbf{0}, i\omega_m = 0) \quad (14)$$

with

$$\begin{aligned} \chi^{2\mathbf{k}_0,e}(\mathbf{k}; \mathbf{q}, i\omega_m) &= \int_0^{\frac{1}{T}} d\tau e^{i\omega_m \tau} \langle T_\tau \Phi^{2\mathbf{k}_0,e}(\mathbf{k}; \mathbf{q}, \tau) \Phi^{2\mathbf{k}_0,e}(\mathbf{k} + \mathbf{q}; -\mathbf{q}, 0) \rangle_{H_0} \\ &= 2 \sum_v \{ \chi_+^v(\mathbf{k}; \mathbf{q}, i\omega_m) + \chi_-^v(\mathbf{k}; \mathbf{q}, i\omega_m) \}, \end{aligned} \quad (15)$$

$$\chi_+^v(\mathbf{k}; \mathbf{q}, i\omega_m) = -T \sum_n G_R^{vv}(\mathbf{k} + \mathbf{q}, i\varepsilon_n + i\omega_m) G_L^{\bar{v}\bar{v}}(\mathbf{k}, i\varepsilon_n), \quad (16)$$

$$\chi_{-}^{\nu}(\mathbf{k}; \mathbf{q}, i\omega_m) = -T \sum_n G_R^{\nu\bar{\nu}}(\mathbf{k} + \mathbf{q}, i\varepsilon_n + i\omega_m) G_L^{\nu\bar{\nu}}(\mathbf{k}, i\varepsilon_n), \quad (17)$$

where λ is the eigenvalue, $\Delta_{\mathbf{k}}$ is the gap, $\bar{\nu} = b(a)$ corresponds to $\nu = a(b)$, $\langle x \rangle_{H_0}$ stands for an ensemble average of the quantity x with respect to the bare Hamiltonian H_0 (Eq. 8) and $\Phi(\mathbf{k}; \mathbf{q}, \tau) = e^{H_0\tau} \Phi(\mathbf{k}; \mathbf{q}) e^{-H_0\tau}$ yields the imaginary time evolution in the interaction representation. (Several superscripts as well as spin indices are omitted for the sake of simplicity; for details, see **Supplemental Discussion A**.) An excitonic condensation occurs when λ reaches unity. Note that the linearized gap equations for other excitonic pairings can be also derived straightforwardly.

The contribution of the inter-node (C_2) fluctuations to the local spin susceptibility for the l th orbital (or the l th molecular site in the unit cell for α -I₃) is calculated by

$$\begin{aligned} \chi_{RL, ll}^{\pm}(\mathbf{q}, i\omega_m) = & \sum_{\mathbf{k}, \nu} [\mathcal{F}_{\nu\nu\bar{\nu}\bar{\nu}}^{RL, ll} \{ \Lambda_{+}^{\nu}(\mathbf{k}; \mathbf{q}, i\omega_m) \chi_{+}^{\nu}(\mathbf{k}; \mathbf{q}, i\omega_m) + \Lambda_{-}^{\nu}(\mathbf{k}; \mathbf{q}, i\omega_m) \chi_{-}^{\nu}(\mathbf{k}; \mathbf{q}, i\omega_m) \} \\ & + \mathcal{F}_{\nu\bar{\nu}\nu\bar{\nu}}^{RL, ll} \{ \Lambda_{-}^{\nu}(\mathbf{k}; \mathbf{q}, i\omega_m) \chi_{+}^{\nu}(\mathbf{k}; \mathbf{q}, i\omega_m) + \Lambda_{+}^{\nu}(\mathbf{k}; \mathbf{q}, i\omega_m) \chi_{-}^{\nu}(\mathbf{k}; \mathbf{q}, i\omega_m) \}], \quad (18) \end{aligned}$$

where the ladder diagram (**Extended Data Fig. 5b**) is given by

$$\begin{aligned} \Lambda_{\pm}^{\nu}(\mathbf{k}; \mathbf{q}, i\omega_m) = & 1 + \sum_{\mathbf{k}'} V_0(\mathbf{k} - \mathbf{k}') [\Lambda_{\pm}^{\nu}(\mathbf{k}; \mathbf{q}, i\omega_m) \chi_{+}^{\nu}(\mathbf{k}'; \mathbf{q}, i\omega_m) \\ & + \Lambda_{\mp}^{\nu}(\mathbf{k}; \mathbf{q}, i\omega_m) \chi_{-}^{\nu}(\mathbf{k}'; \mathbf{q}, i\omega_m)]. \quad (19) \end{aligned}$$

Note that the filled area in the susceptibility diagram (**Extended Data Fig. 5a**) corresponds to $\Lambda_{\pm}^{\nu}(\mathbf{k}; \mathbf{q}, i\omega_m)$. By separating the \mathbf{k} dependence from the $(\mathbf{q}, i\omega_m)$ dependence, one yields $\Lambda_{\pm}^{\nu}(\mathbf{k}; \mathbf{q}, i\omega_m) \simeq \Delta_{\mathbf{k}} \Lambda_{\pm}^{\nu}(\mathbf{q}, i\omega_m) \simeq (1 - \lambda)^{-1}$ at the RPA level using Eq. 14. With decreasing temperature, the transverse spin susceptibility (Eq. 18), and thus $1/T_1 T$ (Eq. 11), increases because a spin fluctuation develops (through the enhancement of the ladder diagram) as a precursor of excitonic condensation, and in turn, diverges at the onset of the condensation (taking place at $\lambda = 1$). The calculated temperature dependence of $1/T_1 T$ is presented in Fig. 4b for the even-parity spin-triplet pairing at $H = 0$ T, which shows an upturn (for $\alpha = 2$) as a direct consequence of this precursor effect.

As to the eigenvalues of the excitonic gap equation, we find that the even-parity, inter-node (C_2), spin transverse instability (described by the eigenvalue λ_{\pm}) develops at low temperatures on increasing the in-plane magnetic field H , whereas the spin longitudinal instability (described by the eigenvalue λ_z) is suppressed with increasing H (**Extended Data Fig. 4**). Moreover, the intra-node (C_1) instability is perceived to be weak compared to the inter-node (C_2) instability (inset of **Extended Data Fig. 4**). (For details, see **Supplementary Discussion B**).

Estimation of the critical temperature and the gap. For the evaluation of the excitonic gap Δ and the critical temperature T_C , we employed Eqs. 1 and 2 together with the cutoff $\Lambda = 0.667 \text{ \AA}^{-1}$ of the size of the inverse lattice constant,³⁹ the permittivity $\epsilon \approx 30$ and the velocity $v = 2.4 \times 10^4 \text{ m s}^{-1}$ determined from the fitting the Knight shift data reported previously.⁹

Additional References in Methods

31. Takano, Y., Hiraki, K., Takada, Y., Yamamoto, H. M. & Takahashi, T. Local spin susceptibility characteristic of zero-gap state of α -(BEDT-TTF)₂I₃ under pressure. *J. Phys. Soc. Jpn.* **79**, 104704 (2010).
32. Hirata, M., Ishikawa, K., Miyagawa, K., Kanoda, K. & Tamura, M. ¹³C NMR study on the charge-disproportionated conducting state in the quasi-two-dimensional organic conductor α -(BEDT-TTF)₂I₃. *Phys. Rev. B* **84**, 125133 (2011).
33. Kakiuchi, T., Wakabayashi, Y., Sawa, H., Takahashi, T. & Nakamura, T. Charge ordering in α -(BEDT-TTF)₂I₃ by synchrotron X-ray diffraction. *J. Phys. Soc. Jpn.* **76**, 113702 (2007).
34. Kawamoto, A., Miyagawa, K., Nakazawa, Y. & Kanoda, K. Electron correlation in the k-phase family of BEDT-TTF compounds studied by ¹³C NMR, where BEDT-TTF is bis(ethylenedithio)tetrathiafulvalene. *Phys. Rev. B* **52**, 15522 (1995).
35. Katayama, S., Kobayashi, A. & Suzumura, Y. Electronic properties close to Dirac cone in two-dimensional organic conductor α -(BEDT-TTF)₂I₃. *Eur. Phys. J. B* **67**, 139–148 (2009).
36. Kawai, T. & Kawamoto, A. ¹³C-NMR study of charge ordering state in the organic conductor, α -(BEDT-TTF)₂I₃. *J. Phys. Soc. Jpn.* **78**, 074711(2009).
37. Hirose, S. & Kawamoto, A. Local spin susceptibility in the zero-gap semiconductor state of α -(BEDT-TTF)₂I₃ probed by ¹³C NMR under pressure. *Phys. Rev. B* **82**, 115114 (2010).
38. Korringa, J. Nuclear magnetic relaxation and resonance line shift in metals. *Physica* **16**, 601-610 (1950).
39. Kondo, R., Kagoshima, S., Tajima, N. & Kato, R. Crystal and electronic structures of the quasi-two-dimensional organic conductor α -(BEDT-TTF)₂I₃ and its selenium analogue α -(BEDT-TSeF)₂I₃ under hydrostatic pressure at room temperature. *J. Phys. Soc. Jpn.* **78**, 114714 (2009).

40. Kobayashi, A., Suzumura, Y. & Fukuyama, H. Hall Effect and Orbital Diamagnetism in Zero-gap State of Molecular Conductor α -(BEDT-TTF)₂I₃. *J. Phys. Soc. Jpn.* **77**, 064718 (2008).
41. Abragam, A. *The Principles of Nuclear Magnetism* (Clarendon, Oxford, 1961).
42. Slichter, C. P. *Principles of Magnetic Resonance*, 3rd ed. (Springer, New York, 1989).
43. Bender, K. et al. Synthesis, structure and physical properties of a twodimensional organic metal, di[bis(ethylenedithio)tetrathiofulvalene]triiodide, (BEDT-TTF)₂⁺I₃⁻. *Mol. Cryst. Liq. Cryst.* **108**, 359–371 (1984).
44. Herring, C. Accidental degeneracy in the energy bands of crystals. *Phys. Rev.* **52**, 365–373 (1937).
45. Asano, K. & Hotta, C. Designing Dirac points in two-dimensional lattices. *Phys. Rev. B* **83**, 245125 (2011).
46. Kobayashi, A., Katayama, S., Noguchi, K. & Suzumura, Y. Superconductivity in charge ordered organic conductor — α -(ET)₂I₃ salt. *J. Phys. Soc. Jpn.* **73**, 3135–3148 (2004).
47. Ishibashi, S., Tamura, T., Kohyama, M. & Terakura, K. Ab Initio Electronic-Structure Calculations for α -(BEDT-TTF)₂I₃. *J. Phys. Soc. Jpn.* **75**, 015005 (2006).
48. Kobayashi, A. & Suzumura, Y. Effects of Zero Line and Ferrimagnetic Fluctuation on Nuclear Magnetic Resonance for Dirac Electrons in Molecular Conductor α -(BEDT-TTF)₂I₃. *J. Phys. Soc. Jpn.* **82**, 054715 (2013).
49. Kobayashi, A., Katayama, S. & Suzumura, Y. Theoretical study of the zero-gap organic conductor α -(BEDT-TTF)₂I₃. *Sci. Technol. Adv. Mater.* **10**, 024309 (2009).
50. Suzumura, Y. & Kobayashi, A. Zero-Gap State in α -(BEDT-TTF)₂I₃ under Hydrostatic Pressure. *J. Phys. Soc. Jpn.* **82**, 044709 (2013).
51. Kondo, R., Kogashima, S. & Harada, J. Crystal structure analysis under uniaxial strain at low

- temperature using a unique design of four-axis x-ray diffractometer with a fixed sample. *Rev. Sci. Instrum.* **76**, 093902 (2005).
52. Mori, T. Requirements for zero-gap states in organic conductors. *J. Phys. Soc. Jpn.* **79**, 014703 (2010).
 53. Mori, T. Zero-Gap States of Organic Conductors in the Presence of Non-Stripe Charge Order. *J. Phys. Soc. Jpn.* **82**, 034712 (2013).
 54. Mori, T. et al. Band structures of two types of (BEDT-TTF)₂I₃. *Chem. Lett.* 957–960 (1984).
 55. Kajita, K. et al. Magnetotransport Phenomena of α -Type (BEDT-TTF)₂I₃ under High Pressures. *J. Phys. Soc. Jpn.* **61**, 23-26 (1992).
 56. Tajima, N., Tamura, M., Nishio, Y., Kajita, K. & Iye, Y. Transport Property of an Organic Conductor α -(BEDT-TTF)₂I₃ under High Pressure - Discovery of a Novel Type of Conductor - *J. Phys. Soc. Jpn.* **69**, 543-551 (2000).
 57. Tajima, N., Sugawara, S., Tamura, M., Nishio, Y. & Kajita, K. Electronic phases in an organic conductor α -(BEDT-TTF)₂I₃: ultra narrow gap semiconductor, superconductor, metal, and charge-ordered insulator. *J. Phys. Soc. Jpn.* **75**, 051010 (2006).
 58. Tajima, N., Sugawara, S., Kato, R., Nishio, Y. & Kajita, K. Effect of the zero-mode Landau level on interlayer magnetoresistance in multilayer massless Dirac Fermion systems. *Phys. Rev. Lett.* **102**, 176403 (2009).
 59. Sugawara, S. et al. Temperature dependence of inter-layer longitudinal magnetoresistance in α -(BEDT-TTF)₂I₃: positive versus negative contributions in a tilted Dirac cone system. *J. Phys. Soc. Jpn.* **79**, 113704 (2010).
 60. Tajima, N. et al. Spin and valley splittings in multilayered massless Dirac fermion system. *Phys. Rev. B* **82**, 121420(R) (2010).
 61. Tajima, N. et al. Quantum Hall effect in multilayered massless Dirac fermion systems with

- tilted cones. *Phys. Rev. B* **88**, 075315 (2013).
62. Osada, T. Surface Transport in the $\nu = 0$ Quantum Hall Ferromagnetic State in the Organic Dirac Fermion System. *J. Phys. Soc. Jpn.* **84**, 053704 (2015).
63. Monteverde, M. et al. Coexistence of Dirac and massive carriers in α -(BEDT-TTF)₂I₃ under hydrostatic pressure. *Phys. Rev. B* **87**, 245110 (2013).
64. Konoike, T., Uchida, K. & Osada, T. Specific heat of the multilayered massless Dirac Fermion system. *J. Phys. Soc. Jpn.* **81**, 043601 (2012).
65. Konoike, T., Sato, M., Uchida, K. & Osada, T. Anomalous Thermoelectric Transport and Giant Nernst Effect in Multilayered Massless Dirac Fermion System. *J. Phys. Soc. Jpn.* **82**, 073601 (2013).
66. Yue, Y. et al. Nonuniform site-charge distribution and fluctuations of charge order in the metallic state of α -(BEDT-TTF)₂I₃. *Phys. Rev. B* **82**, 075134 (2010).
67. Beyer, R. et al. Pressure-dependent optical investigations of α -(BEDT-TTF)₂I₃: Tuning charge order and narrow gap towards a Dirac semimetal. *Phys. Rev. B* **93**, 195116 (2016).
68. Luttinger, J. M. & Kohn, W. Motion of Electrons and Holes in perturbed periodic fields. *Phys. Rev* **97**, 869–883 (1955).
69. Abrikosov, A. A. & Beneslavskii, S. D. Possible existence of substances intermediate between metals and dielectrics. *Sov. Phys. JETP* **32**, 699–708 (1971).
70. González, J., Guinea, F. & Vozmediano, M. A. H. Non-Fermi liquid behavior of electrons in the half-filled honeycomb lattice (a renormalization group approach). *Nucl. Phys. B* **424**, 595–618 (1994).
71. Sheehy, D. E. & Schmalian, J. Quantum critical scaling in graphene. *Phys. Rev. Lett.* **99**, 226803 (2007).
72. Kino, H. & Fukuyama, H. Phase diagram of two-dimensional organic conductors: (BEDT-

- TTF)₂X. *J. Phys. Soc. Jpn.* **65**, 2158–2169 (1996).
73. Seo, H. Charge ordering in organic ET compounds. *J. Phys. Soc. Jpn.* **69**, 805–820 (2000).
 74. Matsuno, G., Omori, Y., Eguchi, T. & Kobayashi, A. Topological Domain Wall and Valley Hall Effect in Charge Ordered Phase of Molecular Dirac Fermion System α -(BEDT-TTF)₂I₃. *J. Phys. Soc. Jpn.* **85**, 094710 (2016).
 75. Schwenk, H. et al. α - and β -(BEDT-TTF)₂I₃ — two modifications with contrasting ground state properties: insulator and volume superconductor. *Mol. Cryst. Liq. Cryst.* **119**, 329–335 (1985).
 76. Wojciechowski, R., Yamamoto, K., Yakushi, K., Inokuchi, M. & Kawamoto, A. High-pressure Raman study of the charge ordering in α -(BEDT-TTF)₂I₃. *Phys. Rev. B* **67**, 224105 (2003).
 77. Jérôme, D., Rice, T. M. & Kohn, W. Excitonic Insulator. *Phys. Rev.* **158**, 472 (1967).
 78. Gorbar, E. V., Gusynin, V. P., Miransky, V. A. & Shovkovy, I. A. Magnetic field driven metal-insulator phase transition in planar systems. *Phys. Rev. B* **66**, 045108 (2002).
 79. Gamayun, O. V., Gorbar, E. V. & Gusynin, V. P. Gap generation and semimetal-insulator phase transition in graphene. *Phys. Rev. B* **81**, 075429 (2010).
 80. Drut, J. E. & Lähde, T. A. Is Graphene in Vacuum an Insulator? *Phys. Rev. Lett.* **102**, 026802 (2009).
 81. González, J. Renormalization group approach to chiral symmetry breaking in graphene. *Phys. Rev. B* **82**, 155404 (2010).
 82. Khveshchenko, D. V. & Leal, H. Excitonic instability in layered degenerate semimetals. *Nucl. Phys. B* **687** [FS], 323-331 (2004).

Acknowledgements

We thank K. Nomura for critical discussions and reading of the manuscript; D. Basko for technical help with RG calculations; M. O. Goerbig for support and discussions; and J. S. Kinyon for fruitful discussions. We also thank discussions with many colleagues, including H. Fukuyama, N. Nagaosa, H. Isobe, H. Kohno, Y. Suzumura, M. Ogata, T. Osada, C. Hotta, H. Yasuoka, D. Liu, H. Nojiri, T. Kihara, M. Potemski, M.-H. Julien, H. Mayaffre and M. Horvatić. This work is supported by MEXT/JSPS KAKENHI (Grant Nos 20110002, 21110519, 24654101, 25220709, 15K05166 and 15H02108), JSPS Postdoctoral Fellowship for Research Abroad (Grant No. 66, 2013) and MEXT Global COE Program at University of Tokyo (Global Center of Excellence for the Physical Sciences Frontier; Grant No. G04). We also acknowledge support from the Kurata Memorial Hitachi Science and Technology Foundation.

Supplementary Information

Supplemental Discussion

A. Excitonic order parameters. Excitonic condensate^{28,77} is a possible ground state which opens a mass gap at the node in the Weyl spectrum. Regarding the excitonic pairings mediated by the long-range Coulomb interaction, extensive studies have been performed for the 2D Weyl fermions (WFs) using various techniques such as mean field,^{5,6,78,79,82} Monte Carlo⁸⁰ and RG approaches.⁸¹ The conclusion there is that the dimensionless Coulomb coupling constant $\alpha = e^2/\epsilon\hbar v_F$ has a critical threshold for the condensate and that the order parameter is strongly momentum dependent near the Weyl nodes. The symmetry breaking induced by the long-range Coulomb interaction have been also studied for the 3D WFs,⁸⁴⁻⁹² where the fundamental physics on the excitonic mass generation is common with 2D except for the effects of the spin-orbit coupling.

For the honeycomb lattice, excitonic orders characterised by a spin-singlet, intra-node and even-parity pairing break the inversion symmetry but not the translational symmetry. Other kinds of orders having nontrivial spin dependence (for spin-triplet pairings) and node dependence (for inter-node pairings or pairings with a node-dependent phase) have been also invoked.⁶ However, all of them are degenerate since all nodes are equivalent and no effects that break this degeneracy have been considered.

Contrary, topologically non-trivial phases have been studied for the half-filled honeycomb lattice with short-range repulsions using a mean-field theory and RG analyses in the framework of the conventional charge density wave (CDW) and spin density wave (SDW).⁸³ The CDW (SDW) state in this model breaks the sublattice-inversion (spin) symmetry while leaving the

lattice translational symmetry intact. The quantum anomalous Hall (QAH) insulator⁹³ breaks the time-reversal symmetry and is characterized by $U(1)$ Chern numbers,⁹⁴ whereas the quantum spin Hall (QSH) insulator⁹⁵ described by Z_2 indices⁹⁶ does not break the time-reversal symmetry.

In the following, we classify various types of order parameters by means of a matrix representation: $\hat{\sigma}_i \otimes \hat{\tau}_j \otimes \hat{s}_k$, where $\hat{\sigma}_i$, $\hat{\tau}_j$, and \hat{s}_k (with the three indices taking one of the four possible values; $i, j, k = 0, x, y, z$) are the unit matrices (for $i, j, k = 0$) and the Pauli matrices (for $i, j, k = x, y, z$) representing the pseudospin, node pseudospin and real spin, respectively. Note that the WF states are described by an 8-component creation operator $\Psi_{\mathbf{k}}^\dagger = (c_{\mathbf{k},s,\eta}^\nu)^\dagger$, where the superscript, the second and third indices of the subscript stand for the two pseudospin bases ($\nu = a, b$), spin ($s = 1(\uparrow), -1(\downarrow)$) and node ($\eta = 1(R), -1(L)$). There are 64 possible order parameters, 8 of which can generate an excitonic mass gap.⁶ In the **Extended Data Table 1**, we list these 8 excitonic order parameters which are categorized with respect to the total momentum referring to the intra-node and inter-node pairings (corresponding to the C_1 and C_2 processes in Fig. 3c), parity and spin in conjunction with the corresponding states for the honeycomb lattice. For instance, for even-parity pairings, these order parameters are derived from Eq. 15 and the linearized gap equation in Eq. 14. Note that \hat{s}_0 ($\hat{s}_{x,y,z}$) corresponds to the spin-singlet (triplet) pairing throughout the following expressions.

The most orthodox order parameter is given by the intra-node (C_1), even-parity operators:

$$\begin{aligned} \Phi^{0,e}(\mathbf{k}; \mathbf{q}) &= \Psi_{\mathbf{k}+\mathbf{q}}^\dagger (\hat{\sigma}_z \otimes \hat{\tau}_0 \otimes \hat{s}_t) \Psi_{\mathbf{k}} \\ &= (c_{\mathbf{k}+\mathbf{q},s,R}^{a\dagger} c_{\mathbf{k},s',R}^a - c_{\mathbf{k}+\mathbf{q},s,R}^{b\dagger} c_{\mathbf{k},s',R}^b + c_{\mathbf{k}+\mathbf{q},s,L}^{a\dagger} c_{\mathbf{k},s',L}^a - c_{\mathbf{k}+\mathbf{q},s,L}^{b\dagger} c_{\mathbf{k},s',L}^b) [\hat{s}_t]_{ss'}, \end{aligned} \quad (20)$$

where \mathbf{k} and $\mathbf{k} \pm \mathbf{q}$ are restricted to the vicinity of a same node. (In the rest of this section, the wavenumber vector \mathbf{q} is assumed to be much smaller compared to the size of the nesting vector $2\tilde{\mathbf{k}}_0$ connecting the two nodes in the first Brillouin zone.) The singlet $\Delta_s^{0,e}$ (triplet $\Delta_t^{0,e}$) order parameter breaks the sublattice-inversion (time-reversal) symmetry, giving rise to a CDW or SDW state for the honeycomb lattice, whereas the lattice translational symmetry remains intact. The Chern number vanishes for both states since the Berry curvatures around the two nodes cancel out. In general, these order parameters can contribute both to the density waves and bond order waves, since the pseudospin bases (corresponding to $\hat{\sigma}_i$) are not always described by the sublattice bases as in graphene but can be generally expressed by the Luttinger-Kohn bases⁶⁸ such as for the 2D tilted WFs in the pressurized α -(BEDT-TTF)₂I₃.^{14,15}

For the intra-node (C₁), odd-parity operators, we can define

$$\begin{aligned}\Phi^{0,o}(\mathbf{k}; \mathbf{q}) &= \Psi_{\mathbf{k}+\mathbf{q}}^\dagger (\hat{\sigma}_z \otimes \hat{\tau}_z \otimes \hat{s}_t) \Psi_{\mathbf{k}} \\ &= (c_{\mathbf{k}+\mathbf{q},S,R}^{a\dagger} c_{\mathbf{k},S',R}^a - c_{\mathbf{k}+\mathbf{q},S,R}^{b\dagger} c_{\mathbf{k},S',R}^b - c_{\mathbf{k}+\mathbf{q},S,L}^{a\dagger} c_{\mathbf{k},S',L}^a + c_{\mathbf{k}+\mathbf{q},S,L}^{b\dagger} c_{\mathbf{k},S',L}^b) [\hat{s}_t]_{ss'}. \quad (21)\end{aligned}$$

In this case, the spin-singlet order parameter $\Delta_s^{0,e}$ breaks the time-reversal symmetry and is well characterized by a $U(1)$ Chern number ($Ch_\uparrow = Ch_\downarrow \neq 0$), while the spin-triplet order parameter $\Delta_t^{0,e}$ has a finite Z_2 index ($Ch_\uparrow - Ch_\downarrow \neq 0$). The corresponding state for the honeycomb lattice is a QAH (QSH) state for the spin-singlet (triplet) case.

For the inter-node (C₂) case, we have even-parity operators:

$$\begin{aligned}
\Phi^{2\mathbf{k}_0,e}(\mathbf{k}; \mathbf{q}) &= \Psi_{\mathbf{k}+\mathbf{q}}^\dagger (\hat{\sigma}_x \otimes \hat{\tau}_x \otimes \hat{s}_t) \Psi_{\mathbf{k}} \\
&= (c_{\mathbf{k}+\mathbf{q},S,R}^{a\dagger} c_{\mathbf{k},S',L}^b + c_{\mathbf{k}+\mathbf{q},S,R}^{b\dagger} c_{\mathbf{k},S',L}^a + c_{\mathbf{k}+\mathbf{q},S,L}^{b\dagger} c_{\mathbf{k},S',R}^a + c_{\mathbf{k}+\mathbf{q},S,L}^{a\dagger} c_{\mathbf{k},S',R}^b) [\hat{s}_t]_{ss'}. \quad (22)
\end{aligned}$$

In the honeycomb lattice, the corresponding spin-singlet (triplet) order parameter $\Delta_s^{2\mathbf{k}_0,e}$ ($\Delta_t^{2\mathbf{k}_0,e}$) represents a charge (spin) bond-order wave, dubbed CBOW (SBOW) hereafter, with a Kekulé pattern.^{97,98} (We note again that these order parameters generally contribute not only to bond-order waves but also to density waves.) The Chern numbers vanish (for both spin singlet and triplet cases) because of the cancellation among the Weyl nodes.

Finally, we can describe the inter-node (C_2), odd-parity operators, which are given by

$$\begin{aligned}
\Phi^{2\mathbf{k}_0,0}(\mathbf{k}; \mathbf{q}) &= \Psi_{\mathbf{k}+\mathbf{q}}^\dagger (\hat{\sigma}_x \otimes \hat{\tau}_y \otimes \hat{s}_t) \Psi_{\mathbf{k}} \\
&= (-ic_{\mathbf{k}+\mathbf{q},S,R}^{a\dagger} c_{\mathbf{k},S',L}^b - ic_{\mathbf{k}+\mathbf{q},S,R}^{b\dagger} c_{\mathbf{k},S',L}^a + ic_{\mathbf{k}+\mathbf{q},S,L}^{b\dagger} c_{\mathbf{k},S',R}^a + ic_{\mathbf{k}+\mathbf{q},S,L}^{a\dagger} c_{\mathbf{k},S',R}^b) [\hat{s}_t]_{ss'}. \quad (23)
\end{aligned}$$

The spin-singlet $\Delta_s^{2\mathbf{k}_0,0}$ and triplet $\Delta_t^{2\mathbf{k}_0,0}$ order parameters correspond to flux states,^{93,94} where these terms provide a mass having an opposite sign for the two nodes.

B. The linearized gap equation for the excitonic instabilities. In **Extended Data Figure 4**, we show the temperature dependence of the eigenvalue λ for the linearized gap equation (Eq. 14), where λ reaches unity at the onset of excitonic condensation. The calculations are performed for the even-parity, spin-triplet excitonic pairings using the Coulomb coupling of $\alpha = 1$. The inset shows the eigenvalues for the intra-node (C_1 in Fig. 3c) and inter-node (C_2) pairings without a

magnetic field. Because the electron-hole symmetry is higher for the C_2 excitonic pairings than for the C_1 excitonic pairings, the C_2 excitonic instability develops stronger on cooling. Upon increasing the in-plane magnetic field, the eigenvalue for the spin transverse instability λ_{\pm} is enhanced, whereas that for the spin longitudinal instability λ_z is suppressed. This is because a perfect nesting exists between the up-spin and down-spin Fermi pockets induced by the field, while the nesting between the same-spin pockets is poor. The odd-parity excitonic orders, which correspond to the topological Mott insulators or the flux states, are expected when the next-nearest neighbour repulsions are larger than the nearest neighbour ones.⁸³ In the present study, however, such exotic orders do not realize since the conventional long-range Coulomb potential ($\propto 1/|\mathbf{r}|$) is considered.

C. The tilted Weyl Hamiltonian and the Form Factor. A standard way to describe non-interacting electrons in solids is to use a tight-binding model such as^{13,46}

$$H_0 = \sum_{\langle il;jm \rangle} (t_{il;jm} c_{il}^{\dagger} c_{jm} + \text{h.c.}), \quad (24)$$

where i, j ($= 1, \dots, N$) label the different unit cells and l, m denote the orbitals (for α -(BEDT-TTF)₂I₃, they correspond to the molecular sites A, A', B and C in Fig. 1a). By using the Fourier transformation, $c_{i\alpha} = N^{1/2} \sum_{\mathbf{k}} e^{i\mathbf{k} \cdot \mathbf{r}_i} c_{\mathbf{k}l}$, the Hamiltonian is written as

$$H = \sum_{\mathbf{k}, l, m} H_{lm}(\tilde{\mathbf{k}}) c_{\mathbf{k}l}^{\dagger} c_{\mathbf{k}m}, \quad (25)$$

where $H_{lm}(\tilde{\mathbf{k}})$ is given by the Fourier transform of the transfer integral $t_{il;jm}$. The eigenvalue equation is given by

$$\sum_m H_{lm}(\tilde{\mathbf{k}}) d_{m\xi}(\tilde{\mathbf{k}}) = \varepsilon_\xi(\tilde{\mathbf{k}}) d_{m\xi}(\tilde{\mathbf{k}}), \quad (26)$$

where $\varepsilon_\xi(\tilde{\mathbf{k}})$ is the eigenvalue with the band index ξ . We assume that the conduction and valence bands are degenerated at the Weyl nodes (at $\pm\tilde{\mathbf{k}}_0$), where $\tilde{\mathbf{k}}_0$ is a general momentum defined in the first Brillouin zone. We also assume that the Fermi energy E_F is fixed at the nodes such as have been known for the 3/4-filled system α -(BEDT-TTF)₂I₃ under pressure.^{13,14}

To obtain an effective Hamiltonian describing the low-temperature WF states in α -(BEDT-TTF)₂I₃, we move to the Luttinger-Kohn (LK) representation⁶⁸ and expand the Hamiltonian around the nodes.¹⁴ The LK bases are given by using the Bloch periodic functions with a fixed wavevector. Here we choose a fixed wavevector $\tilde{\mathbf{k}}'_0$ which locates in the vicinity of the Weyl node $\tilde{\mathbf{k}}_0$ but has slightly shifted from the node. This is to avoid the singularity of the wave function $d_{m\xi}(\tilde{\mathbf{k}})$, where $d_{m\xi}(\tilde{\mathbf{k}})$ is given by a (normalized) superposition of the highest occupied molecular orbital (HOMO) on each of the four different BEDT-TTF molecules in the unit cell (see Fig. 1a). Note that WFs around $\tilde{\mathbf{k}}_0$ ($\eta = R$: the right node) can be distinguished from those around $-\tilde{\mathbf{k}}_0$ ($\eta = L$: the left node) – the so-called node degrees of freedom. Around the right node, the expansion reads

$$\sum_{lm} d_{l\xi}^*(\tilde{\mathbf{k}}'_0) H_{lm}(\tilde{\mathbf{k}}) d_{m\xi'}(\tilde{\mathbf{k}}'_0) \simeq \sum_{lm} d_{l\xi}^*(\tilde{\mathbf{k}}'_0) \left\{ \left[\frac{\partial H_{lm}(\tilde{\mathbf{k}})}{\partial \tilde{\mathbf{k}}} \right]_{\tilde{\mathbf{k}}=\tilde{\mathbf{k}}'_0} \cdot \mathbf{k} \right\} d_{m\xi'}(\tilde{\mathbf{k}}'_0), \quad (27)$$

where the wavenumber vector $\tilde{\mathbf{k}}$ resides in the first Brillouin zone, while \mathbf{k} is measured from the Weyl node $\tilde{\mathbf{k}}_0$: $\mathbf{k} = \tilde{\mathbf{k}} - \tilde{\mathbf{k}}_0$. At low energy, one can construct an effective two-band model for each node, where the dispersion is liner around each of the nodes with a high energy cutoff. Herewith, we obtain the tilted Weyl Hamiltonian:^{14,15}

$$H_0 = \hbar(\mathbf{w} \cdot \mathbf{k} \hat{\sigma}_0 \otimes \hat{t}_z + v_x k_x \hat{\sigma}_x \otimes \hat{t}_z + v_y k_y \hat{\sigma}_y \otimes \hat{t}_0). \quad (28)$$

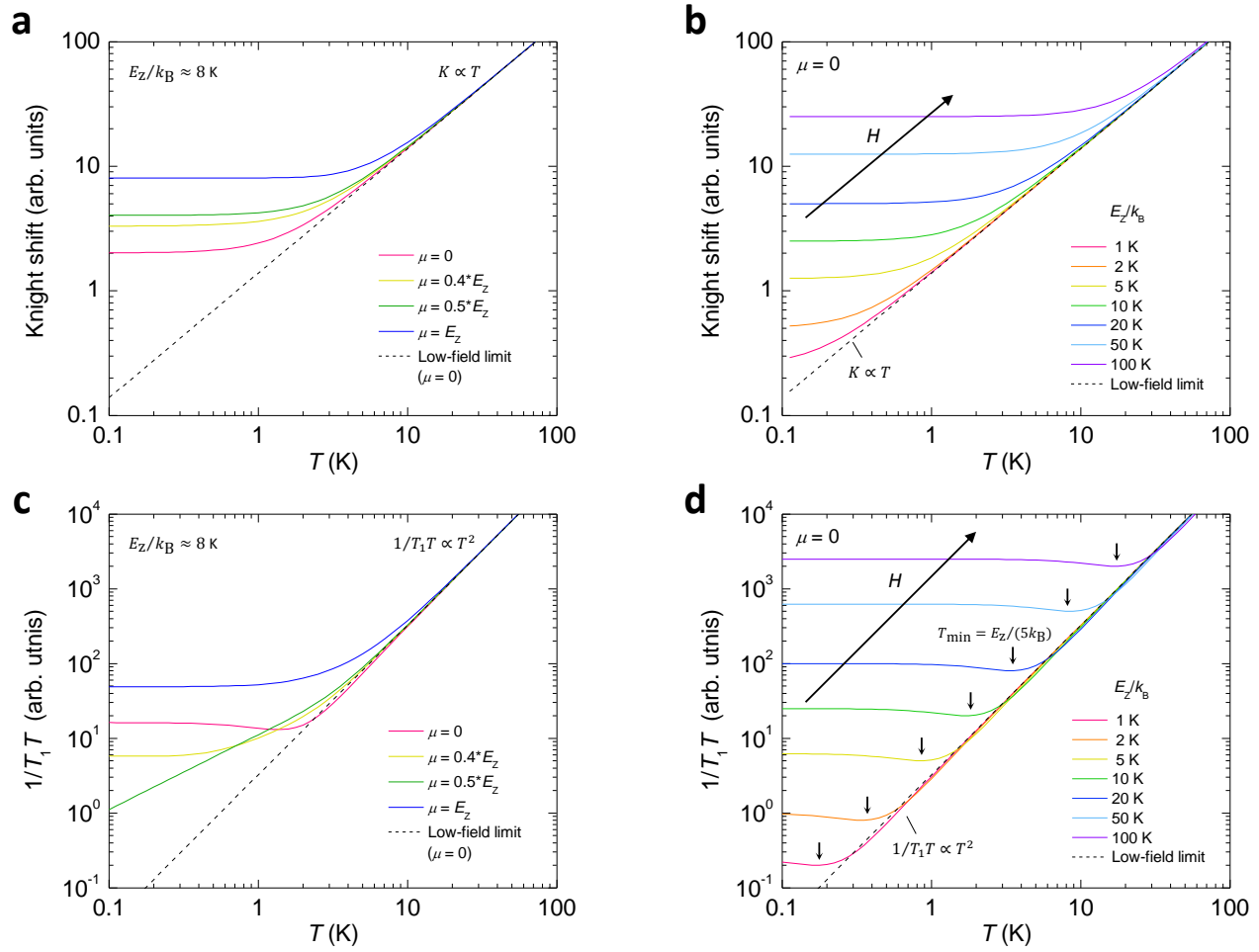
The form factor in Eqs 12 and 13 is expressed by using the LK bases as

$$\mathcal{F}_{\nu_1, \nu_2, \nu_3, \nu_4}^{\eta, \eta', l, m} = d_{l\nu_1}(\eta \tilde{\mathbf{k}}'_0) d_{m\nu_2}^*(\eta \tilde{\mathbf{k}}'_0) d_{m\nu_3}(\eta' \tilde{\mathbf{k}}'_0) d_{l\nu_4}^*(\eta' \tilde{\mathbf{k}}'_0). \quad (29)$$

References

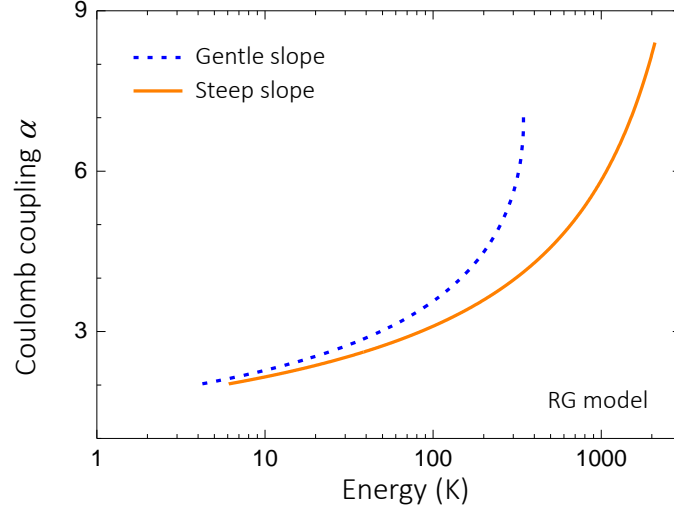
83. Raghu, S., Qi, X.-L., Honerkamp, C. & Zhang, S.-C. Topological Mott Insulators, *Phys. Rev. Lett.* **100**, 156401 (2008).
84. Wei, H., Chao, S.-P. & Aji, V. Excitonic Phases from Weyl Semimetals. *Phys. Rev. Lett.* **109**, 196403 (2012).
85. Sekine, A. & Nomura, K. Weyl Semimetal in the Strong Coulomb Interaction Limit. *J. Phys. Soc. Jpn.* **83**, 094710 (2014).
86. Wei, H., Chao, S.-P. & Aji, V. Long-range interaction induced phases in Weyl semimetals. *Phys. Rev. B* **89**, 235109 (2014).
87. Sekine, A. & Nomura, K. Stability of multinode Dirac semimetals against strong long-range correlations. *Phys. Rev. B* **90**, 075137 (2014).

88. Maciejko, J. & Nandkishore, R. Weyl semimetals with short-range interactions. *Phys. Rev. B* **90**, 035126 (2014).
89. Buividovich, P. V. Spontaneous chiral symmetry breaking and the chiral magnetic effect for interacting Dirac fermions with chiral imbalance. *Phys. Rev. D* **90**, 125025 (2014).
90. Roy, B. & Sau, J. D. Magnetic catalysis and axionic charge density wave in Weyl semimetals. *Phys. Rev. B* **92**, 125141 (2015).
91. Laubach, M., Platt, C., Thomale, R., Neupert, T. & Rachel, S. Density wave instabilities and surface state evolution in interacting Weyl semimetals. *Phys. Rev. B* **94**, 241102(R) (2016).
92. Roy, B. & Das Sarma, S. Quantum phases of interacting electrons in three-dimensional dirty Dirac semimetals. *Phys. Rev. B* **94**, 115137 (2016).
93. Haldane, D. M. Model for a Quantum Hall Effect without Landau Levels: Condensed-Matter Realization of the "Parity Anomaly". *Phys. Rev. Lett.* **61**, 2015 (1988).
94. Thouless, D. J., Kohmoto, M., Nightingale, M. P. & den Nijs, Quantized Hall Conductance in a Two-Dimensional Periodic Potential. *Phys. Rev. Lett.* **49**, 405 (1982).
95. Kane, C. L. & Mele, E. J. Quantum Spin Hall Effect in Graphene. *Phys. Rev. Lett.* **95**, 226801 (2005).
96. Kane, C. L. & Mele, E. J. Z_2 Topological Order and the Quantum Spin Hall Effect. *Phys. Rev. Lett.* **95**, 146802 (2005).
97. Hou, C.-Y. H., Chamon, C. & Mudry, C. Electron Fractionalization in Two-Dimensional Graphenelike Structures. *Phys. Rev. Lett.* **98**, 186809 (2007).
98. Gutiérrez, C. et al. Imaging chiral symmetry breaking from Kekulé bond order in graphene. *Nat. Physics* **12**, 950–958 (2016).



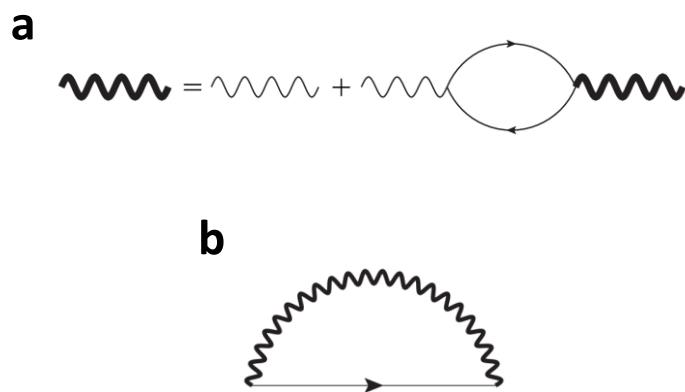
Extended Data Figure 1 | Influences of the electron Zeeman effect and self-doping on the T dependence of the Knight shift and $1/T_1T$. a-d; Calculated profiles of the Knight shift K [(a) and (b)] and $1/T_1T$ [(c) and (d)] in terms of the DOS approximation are plotted against temperature for a non-interacting Weyl cone with electron-hole symmetry. Calculated curves for various values of the chemical potential μ and magnetic field H are presented, where the T dependence of μ is omitted. In (a) and (c), the μ dependence of the curves is shown for $H = 6$ T (corresponding to the electron Zeeman energy of $E_z/k_B = g\mu_B H/k_B \approx 8$ K), while the H dependence is shown in (b) and (d) for $\mu = 0$. ($E = 0$ stands for the band-crossing point) The dashed lines reflect $K \propto T$ and $1/T_1T \propto T^2$ that one obtains in the low-field limit for $\mu = 0$.^{27,35}

The small arrows in **(d)** indicate the positions of $1/T_1 T$ minimum, where the minimum temperature T_{\min} scales to E_Z : $T_{\min} = E_Z/(5k_B)$. K and $1/T_1 T$ level off typically below T_{\min} .

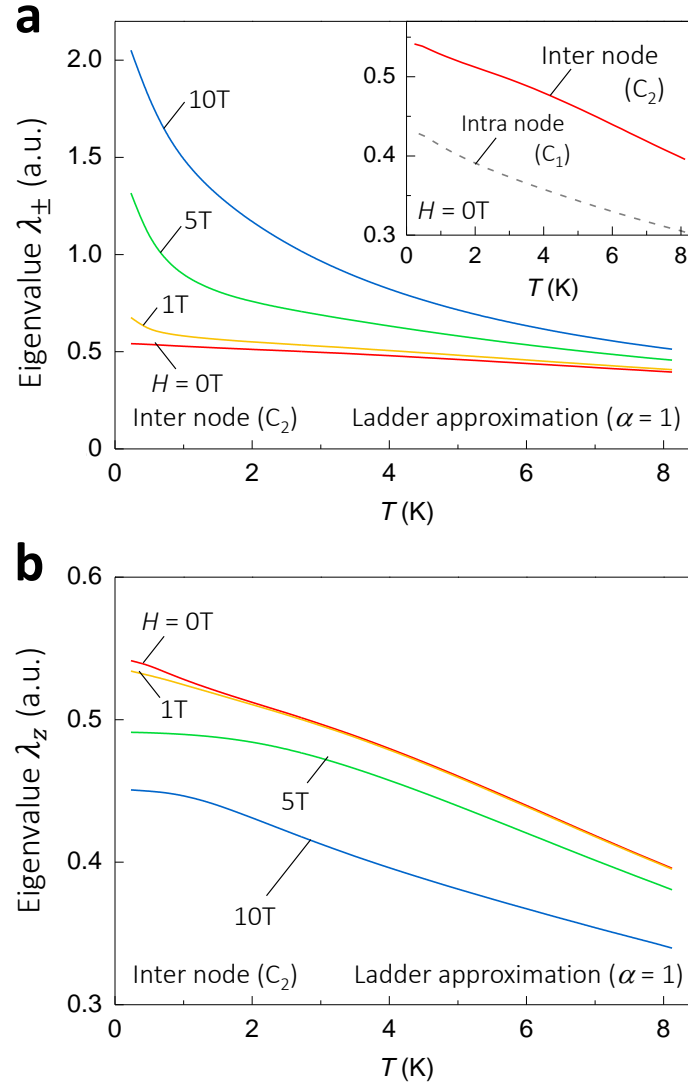


Extended Data Figure 2 | Anisotropic RG flow of the Coulomb coupling in

α -(BEDT-TTF)₂I₃. Parameters used for the calculation are $\varepsilon \approx 30$ and the velocity $v = 2.4 \times 10^4$ m s⁻¹ determined from fitting the Knight shift data using RG analyses, whose details are described in Ref. 9 (see **Methods**). The dimensionless Coulomb coupling α , which is highly anisotropic around the Weyl node reflecting the tilt of the Weyl cone in α -(BEDT-TTF)₂I₃, is evaluated at the gentle slope (dashed trace) and the steep slope (solid trace) of the tilted cone.

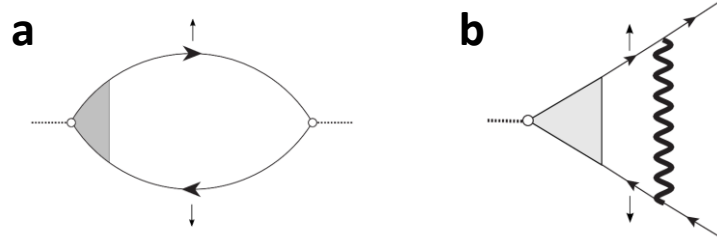


Extended Data Figure 3 | Diagrams employed in the RG calculation. a-c, Feynman diagrams used in the RG calculations. Dressed boson propagator for the random phase approximation (RPA) (bold wavy line) (**a**) and the electron self-energy (**b**).



Extended Data Figure 4 | Eigenvalues for the excitonic pairings. The temperature dependence of the eigenvalue of the linearized gap equation (Eq. 14) for the even-parity, spin-triplet excitonic pairings derived from the ladder approximation with the velocity renormalization considered (see **Methods**). The dimensionless Coulomb coupling of $\alpha = 1$ is employed in the calculation. **a**, The eigenvalues for the spin transverse instability λ_{\pm} (**a**) and the spin longitudinal instability λ_z (**b**) for the inter-node pairing (C_2 in Fig. 3c) are plotted calculated using the in-plane magnetic field H of 0 T (red), 1 T (orange), 5 T (green) and 10 T (blue). At $H = 0$, λ_{\pm} and λ_z are degenerate,

while λ_{\pm} grows towards lower temperature much stronger than λ_z at a finite field. Note that the excitonic condensation appears above $\lambda = 1$. Inset of **a**: Eigenvalues for the intra-node (C_1 in Fig. 3c) and inter-node (C_2) pairings at $H = 0$.



Extended Data Figure 5 | Spin susceptibility and Ladder diagram. Feynman diagrams for the spin susceptibility (Eq. 18) **(a)** and the ladder diagram $\Lambda_+^V(\mathbf{k}; \mathbf{q}, i\omega)$ (Eq. 19) **(b)**. The renormalized fermion propagator due to the self-energy effect (bold line) and the RPA boson propagator (wavy line) shown in **Extended Data Figs 3a** and **3b** are incorporated.

Order parameter	Momentum	Parity	Spin	Matrix	State for honeycomb
$\Delta_s^{0,e}$	0	Even	Singlet	$\hat{\sigma}_z \otimes \hat{\tau}_0 \otimes \hat{s}_0$	CDW
$\Delta_t^{0,e}$	0	Even	Triplet	$\hat{\sigma}_z \otimes \hat{\tau}_0 \otimes \hat{s}_{x,y,z}$	SDW
$\Delta_s^{0,o}$	0	Odd	Singlet	$\hat{\sigma}_z \otimes \hat{\tau}_z \otimes \hat{s}_0$	QAH
$\Delta_t^{0,o}$	0	Odd	Triplet	$\hat{\sigma}_z \otimes \hat{\tau}_z \otimes \hat{s}_{x,y,z}$	QSH
$\Delta_s^{2k_0,e}$	$2\mathbf{k}_0$	Even	Singlet	$\hat{\sigma}_x \otimes \hat{\tau}_x \otimes \hat{s}_0$	CBOW
$\Delta_t^{2k_0,e}$	$2\mathbf{k}_0$	Even	Triplet	$\hat{\sigma}_x \otimes \hat{\tau}_x \otimes \hat{s}_{x,y,z}$	SBOW
$\Delta_s^{2k_0,o}$	$2\mathbf{k}_0$	Odd	Singlet	$\hat{\sigma}_x \otimes \hat{\tau}_y \otimes \hat{s}_0$	Flux
$\Delta_t^{2k_0,o}$	$2\mathbf{k}_0$	Odd	Triplet	$\hat{\sigma}_x \otimes \hat{\tau}_y \otimes \hat{s}_{x,y,z}$	Flux

Supplementary Data Table 1 | Classification table for possible excitonic order parameters.

Also presented are the parity, spin, matrix representation and the corresponding states in the honeycomb lattice,⁶ where $\hat{\sigma}_i$, $\hat{\tau}_j$, and \hat{s}_k ($i, j, k = 0, x, y, z$) are the Pauli matrices representing the pseudospin, real spin and node pseudospin, respectively. The index 0 stands for the 2×2 unit matrices. Here, CDW (SDW) indicates a charge (spin) density wave, QAH (QSH)⁸⁴ stands for a quantum anomalous Hall (quantum spin Hall) state and CBOW (SBOW)⁹⁸ represents a charge (spin) bond-order wave.